

Utilizing LAMMPS to Simulate Rod-like Colloid Nematic Phases.



Physical and Theoretical Chemistry Teaching Laboratory, Department of
Chemistry, University of Oxford.

Honour school of Chemistry, part II project
by Joseph Daws

June 9, 2023

Everything should be made as simple as possible, but not simpler.

Albert Einstein

It ain't what you don't know that gets you into trouble. It's what you know for sure that just ain't so.

Mark Twain

Abstract

This thesis focuses on applications of molecular dynamics (MD) simulations to systems of rod-like colloids + polymer. The motivation for this research is to further understand the phase behaviour of colloidal rods in the presence of non-interacting polymer and enhance our understanding of LC droplets observed in experimentation and the lungs of Cystic Fibrosis patients.

The study of rods + polymer and tactoids using MD is relatively novel and this thesis will help to further applications of MD in soft matter systems.

Acknowledgements

Firstly, I would like to thank my supervisor, Dirk Aarts, for the opportunity to research in an area which has always been of great interest to me and for his superb 3rd year lecture courses in Soft Condensed Matter and an Introduction to the Liquid State, which entertained and inspired me.

I also want to give a special thanks to the whole Oxford Colloid Group in particular Callum, Clare, Jack, Mohammed and Shivani for their help and support. I would like to further give thanks to Dr Martin Galpin for help with a number of geometric problems and also Eryk for his guidance with LAMMPS during periods where I was lost or confused.

This year has been one of the most interesting and enjoyable of my education and has inspired me to continue computer programming, a prospect that would have shocked me 4 years ago.

Last, but not least, I would like to thank my family for their support, especially through the tough periods of my degree.

Contents

Abstract	ii
Acknowledgements	iii
Glossary	vii
List of Figures	xi
List of Tables	xv
1 Introduction	1
1.1 The Colloidal Domain	1
1.1.1 The Depletion Interaction	1
1.1.2 Rods and Liquid Crystals	2
1.1.3 Rod-like Colloids and the Depletion Interaction	2
1.2 Biological Motivation: Cystic Fibrosis	3
1.3 Molecular Dynamics	4
1.4 Scope and Outline of this Thesis	5
2 Theory	7
2.1 Molecular Dynamics	7
2.1.1 A basic approach to MD	7
2.1.2 MD: Initialization, Force Calculation and Integrating Newton's Equations	8
2.1.3 Langevin Dynamics and the Canonical Ensemble	9
2.1.4 LAMMPS	10
2.2 Phase behaviour of Rods and Depletant	11

2.2.1	The Depletion Interaction	11
2.2.2	Free Volume Theory	13
2.2.3	Onsager's Theory for Infinity Thin Rigid Hard Rods	15
2.2.4	The Phase Behaviour of Finite Rigid Rods with Penetrable Hard Spheres	19
3	Modelling and Simulations	23
3.1	System Modelling	23
3.1.1	Modelling of Rigid Rods	23
3.1.2	Modelling the Cell	24
3.1.3	Modelling the Depletion Interactions using the Lennard-Jones Potential	25
3.1.4	Cell Interactions	28
3.2	LAMMPS Implementation of Molecular Dynamics	28
3.2.1	Initialization	28
3.2.2	Factors to consider in the LAMMPS Input File.	29
3.3	Monitoring the Simulation	30
3.3.1	Measuring Order - Order Parameter Calculation	30
3.3.2	Collecting Thermodynamic Data	32
3.3.3	Establishing Equilibrium	32
3.3.4	System Visualization	33
4	Results & Discussion	34
4.1	Rods and the Depletion Interaction	34
4.1.1	The Theoretical Isotropic-Nematic Phase Diagrams	34
4.1.2	The MD Phase Behaviour of Attractive Rigid Rods	37
4.1.3	Comparing MD and Theory	41
4.1.4	Comparing MD Results to previous Simulation work	43
4.1.5	Comparing MD and Experimental Phase Behaviour	44
4.1.6	Summary for Rod + Depletant Systems	47

4.2	Generating Tactoids in MD	47
4.2.1	Imaging of Tactoids in Rod-like Colloid Isotropic Phases	48
4.2.2	Generating Tactoids under Different Conditions	50
4.2.3	Comparing MD and Experimental Tactoids	52
4.2.4	Summary of our Tactoids	54
5	Conclusion and Outlook	55
5.1	Chapter Summary	55
5.2	Outline of Results	55
5.3	Future Work	56
Bibliography		57
A	Integrating Newton's Equations of Motion.	61
B	The Volume of Overlap of Two Parallel Rods.	64
C	Scaled Particle Theory of Finite Sized Rods	66
D	LAMMPS Data Generator File	69
E	LAMMPS Input Scripts	71
F	The Critical Endpoint	76

Glossary

List of Symbols

α	Volume over free volume ratio
$\mathbf{a}(t)$	acceleration at time, t
b	excluded volume of an infinitely thin rod
B_2	Second virial coefficient
B_3	Third virial coefficient
c	The dimensionless concentration
d	Dimension
ϵ	Well depth
η	Viscosity coefficient
f	The orientation distribution function
f_G	The Gaussian orientational distribution function
F	Helmholtz free energy
h	Timestep or Separation distance
κ	Variational minimization constant
k_b	Boltzmann constant
λ	particle scaling parameter
L	Rod cylinder length
L_t	Total Rod length
μ	Chemical potential
μ_d	Chemical potential of depletant
n_b	Bulk number density
n_d	System number density of depletants

n_d^R	Reservoir number density of depletants
n_r	Number density of rods
N	Number
\mathcal{N}	Number of systems in an ensemble
N_r	Number of rods
N_d	Number of depletants
ω, ω'	Rod orientations
$\hat{\Omega}$	Semi-grand potential
P	Pressure
P_{bulk}	Bulk pressure
P^R	Reservoir pressure
P_2	Second Legendre polynomial
ϕ	Volume fraction
ϕ_d	Volume fraction of depletant
$\phi_{d,R}$	Volume fraction of depletant in reservoir
ϕ_r	Volume fraction of rods
ψ_6	Hexatic order parameter
q	Aspect ratio
R	Radius
$\rho[f]$	Packing entropy per particle
σ_d	diameter of depletant
$\sigma[f]$	Per particle orientational entropy
σ_r	diameter of rod
SLJ	Summed Lennard-Jones
S_2	Nematic order parameter
s_{or}	Orientational entropy
T	Temperature
τ	Smectic order paramter
$\tau(t)$	position at time, t

θ	angle
U	Interaction potential
v	Velocity
V	Volume
$\langle V_{\text{free}} \rangle$	Free volume in the system
$\langle V_{\text{free}} \rangle_0$	Free volume in a pure rod dispersion
ν_0	Rod volume
ν_{excl}	excluded volume
W	Work done
ξ	Stokes' coefficient

List of Acronyms

CPU	Central Processing Unit
CF	Cystic Fibrosis
CFTR	fibrosis transmembrane conductance regulator
EPS	Extracellular Polymer Matrix
FVT	Free Volume Theory
GPU	Graphical Processing Unit
hs	hard sphere
I	Isotropic
IUPAC	The International Union of Pure and Applied Chemistry
KE	Kinetic Energy
N	Nematic
PE	Potential Energy
phs	penetrable hard sphere
LAMMPS	Large Atomic/Molecular Massively Parallel Simulator
LC	Liquid Crystal
LD	Langevin Dynamics
LJ	Lennard-Jones

MD	Molecular Dynamics
MPI	Message Passing Interface
<i>P.Aeruginosa</i>	<i>Pseudomonas Aeruginosa</i>
SEM	Scanning Electron Microscopy
SPT	Scaled Particle Theory
TE	Total Energy
TMV	Tobacco Mosaic Virus
VMD	Visual Molecular Dynamics
WCA	Weeks-Chandler-Anderson
WHO	World Health Organisation

List of Figures

1.1	This Figure illustrates the common phases of rod-like colloids including: Isotropic, Nematic, Smectic A, Smectic C, Columnar and Crystalline.	3
1.2	This Figure [1] are confocal microscopy images of tactoids formed from systems of Pf4 virus and sodium alginate. The scale bar is $20 \mu\text{m}$	4
2.1	This Figure illustrates the FVT setup, here we consider a system of penetrable hard sphere polymers and rod-like colloids attached to a reservoir of polymers through a semi-permeable membrane, that only the penetrable hard sphere polymer can move between.	13
3.1	This Figure shows the model for the Pf4 virus and <i>P.Aeruginosa</i> . I is the 21 particle rod, II is the 31 particle rod, III is the 11 particle long cell and IV is the 4 particle short cell. L = Cylinder length, L_t = Total length, D = Diameter and h = separator distance. See Table 3.1 for dimensions and properties of I-IV.	24
3.2	This Figure shows the fitting of the depletion interaction to the SLJ potential for the 21 and 31 particle rods, for $\epsilon = 0.01k_bT$	27
3.3	This Figure shows an example initialization system. (a) is a side on view showing the stacking of rods in the crystalline stack. (b) shows a perspective view of an initial system with the simulation box outline.	28

4.1 This Figure is the isotropic-nematic phase diagrams for a system of rods + depletant with system variables found in Table 4.1. (a) is the reservoir diagram plotting reservoir polymer volume fraction against rod volume fraction. (b) is the system diagram showing system polymer volume fraction against rod volume fraction. The black and orange lines are the binodals and the blue lines are tie lines. Note the tie lines for the reservoir plot are not shown as they are parallel to the rod volume fraction axis.	36
4.2 This Figure shows the 4 pure phases observed in our MD. (a) is the crystalline/smectic A phase, (b) is the smectic C phase, (c) is the nematic phase and (d) is the isotropic phase. The average S_2 parameters are shown on the diagram. Indicated on the Figure is a crystalline layer, a cavity and a smectic C layer.	39
4.3 This Figure shows the 4 observed biphasic regions. (a) is the aligned isotropic, (b) is the isotropic + nematic coexistence, (c) is the isotropic + smectic coexistence and (d) is the smectic cluster phase. The average S_2 parameters are shown on the diagram. Indicated on the Figure our regions of smectic clusters, isotropic phases and local ordering.	40
4.4 This Figure overlays the MD points tested on the theoretical phase diagram in Figure 4.1 (b). I, II, III, IV are regions outlined by the grey boxes, these refer to the 4 regimes in Table 4.4.	42
4.5 This Figure is taken from [2] with the figure description. (a) <i>Snapshot of simulated system. The spherical beads forming the rods are represented in gray. Depletant particles are represented by orange beads.</i> (b) <i>Frequent assemblies observed in simulations.</i>	45
4.6 This Figure is the experimental phase diagram of [1]. (a) is the experimental phase diagram, (b) is an example isotropic phase, (c) is an example tactoid phase and (d) is an example network phase. The scale bar is $20\mu m$	46

4.7 This Figure [1] shows the observed network structures. (a) is a cartoon image of the tactoid aligning in networks and (b) is a network image. The scale bar is $20\mu m$	46
4.8 This Figure shows multiple images of the long cell tactoids and experimental tactoids. (a) SEM Images from [3](ai) vanadium pentoxide [4], (aii) aluminium oxyhydroxide [5], (aiii) TMV [6] and (aiv) schematic of nematic tactoids with homogeneous, intermediate and bipolar director field configurations formed in carbon nanotube dispersions [7]. (b) Image of long cell tactoid and isotropic coexistence, (c) and (d) close up images of tactoids. Example regions of nematic/smectic clustering are labelled in (b-d).	49
4.9 This Figure shows close up images of tactoid for comparison with experimental tactoids. (a-d) Images of MD tactoids from different perspectives, (e) theoretical and experimental SEM images of nematic tactoids [8] and (f) theoretical and experimental SEM images of smectic tactoids [8].	50
4.10 This Figure shows the tactoid formation under 3 different depletant concentrations. (a) $\phi_d = 0$, (b) $\phi_d = 0.25$ and (c) $\phi_d = 0.5$	51
4.11 This Figures shows images from different cell-rod LJ ϵ values. (a) and (c) $\epsilon = 0.3$. (b) and (d), $\epsilon = 2.0$. (a) and (b) are side on tactoid images. (c) and (d) are cross-sectional views. Some regions of rod-cell alignment and smectic/nematic clusters are indicated on the diagram.	52
4.12 This Figure shows the MD, experimental and theoretical tactoid shapes expected. (a) is a birds-eye-view image taken from my tactoid simulations, (b) is an image of an experimental tactoid from [1] at the following: Pf4 (mg/mL) = 1 and Sodium alginate (mg/mL) = 2.5 and (c) is an image of a typical theoretical tactoid with cell encapsulation, taken from Figure 5.4 of [1].	53
B.1 This Figure shows the cross-sectional slice of Figure B.2	64
B.2 This Figure displays the depletion overlap volume of two parallel cylinders.	65

List of Tables

2.1	This Table compares the output coexistence concentrations and S_2 values for solving the coexistence condition using numerical methods, Onsager's trial function and Odijk's Gaussian trial function. S_2 is the nematic order parameter, see Section 3.3.1.	17
2.2	This Table summarises the important equations from the SPT of finite rods, Appendix C.	20
2.3	This Table gives the meaning of a , b and c in (2.56).	21
3.1	This Table shows the dimensions and properties of the cells and rods detailed in Figure 3.1. As well as the dimensions of Pf4 virus.	25
4.1	This Table displays the dimensions and properties of the rod-depletant system.	35
4.2	This Table summaries the average S_2 values for the pure and biphasic systems. $\Delta S_2 = \max(S_2) - \min(S_2)$	41
4.3	This Table describes the main MD regions of ϕ_r illustrated in Figure 4.4 by grey transparent bars.	43
4.4	This Table provides a comparison of my MD results to the MC results of Bolhuis et al [10].	44
4.5	This Table compares the properties of our system with those of Calero et al [2].	44

Chapter 1

Introduction

This chapter begins by discussing the colloidal domain and depletion interaction. We then discuss rod-like colloids and liquid crystals and how they are influenced by the depletion interaction. Following this we discuss the biological motivation of liquid crystal droplet formation in cystic fibrosis patients and introduce the technique known as molecular dynamics (MD) that will be used to investigate rod-like colloidal systems and liquid crystal formation.

1.1 The Colloidal Domain

Colloidal particles are defined according to the International Union of Pure and Applied Chemistry (IUPAC) as a state of subdivision implying that the molecules or poly-molecular particles dispersed in a medium have at least in one direction a dimension roughly between 1 nm and 1 μm , or that in a system discontinuities are found at distances of that order [11]. Colloidal suspensions exhibit staggering properties. Dispersion such as these were observed over 150 years ago by Faraday (1856) [12] as a colloidal gold sol which persists almost indefinitely yet collapses rapidly and irreversibly upon the addition of salt solution [13].

1.1.1 The Depletion Interaction

In the presence of non-adsorbing polymer/particles, colloids experience an effective attraction, called the depletion interaction. This interaction has been observed for centuries, some examples include the creaming of latex and aggregation of red blood cells [9]. Prior to the theory of Asakura and Oosawa (1950s) [14] the origin of the depletion interaction

was not understood. We now know the depletion interaction arises from osmotic pressure of non-absorbing polymer forcing the colloidal particles together and in turn maximising configurational entropy of the polymers, this is a purely entropic effect and is often observed in system where all direct particle-particle interactions are repulsive [15]. For a historical and theoretical account of the depletion interaction, see [9]. The depletion interaction is commonly observed in systems involving rod-like colloids. Before discussing the depletion interaction with rod-like colloids, we shall discuss rod-like colloid phase behaviour.

1.1.2 Rods and Liquid Crystals

Rod-like colloidal particles exhibit lyotropic Liquid Crystal (LC) phase behaviour [16]. For rods of $L/D \geq 3.5$ at different volume fractions, we observe a wide range of phases including isotropic, nematic, smectic, columnar and crystalline, see Figure 1.1. These phases assemble in systems of repulsive rods indicating that this phase behaviour is of entropic origin as demonstrated by Onsager's theory [15]. LC rod-like suspensions were first observed in suspensions of inorganic colloids, V_2O_5 , by Zocher et al in 1925 [9]. Examples in nature include tobacco mosaic virus [17] and cell/biological membranes [18]. The isotropic-nematic phase transition in rod-like colloidal suspensions is observed due to the balancing of two types of entropy: packing entropy and orientational entropy [15]. At low volume fraction (ϕ), the maximisation of the orientational entropy leads to preferential stability of the isotropic phase. As ϕ increases, we begin to favour maximising packing entropy at the cost of orientational entropy. The gain in packing entropy for larger ϕ outweighs the reduction in the orientational entropy and stabilises the nematic phase.

1.1.3 Rod-like Colloids and the Depletion Interaction

While the phase behaviour of polymer and monodisperse spherical colloids has been studied extensively [9], the self-assembly of rod-like colloids in the presence of polymer has been the subject of more recent study. Recent experimentation in this field includes work by Park et al [19] into depletion induced shape and size selection of gold rods and cubes and Baranov et al [20] who showed that the depletion interaction were effective in the shape selection of $CdSe/CdS$ -rods from a mixture of rods and $CdSe$ spheres.

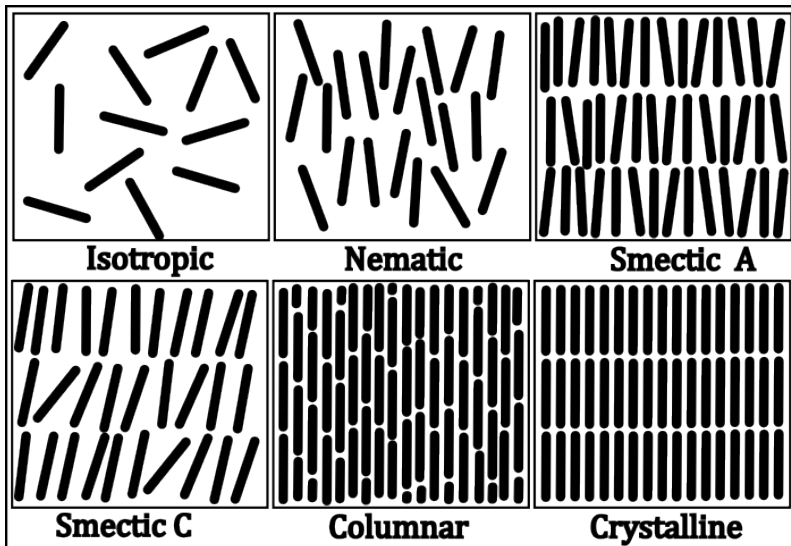


Figure 1.1: This Figure illustrates the common phases of rod-like colloids including: Isotropic, Nematic, Smectic A, Smectic C, Columnar and Crystalline.

1.2 Biological Motivation: Cystic Fibrosis

Cystic Fibrosis (CF) is a life-threatening genetic condition caused by a specific mutation in the gene that encodes fibrosis transmembrane conductance regulator (CFTR) protein. CF affects approximately 70,000 people worldwide [21].

While the exact cause of CF as a consequence of CFTR dysfunction is not yet known, it is evident that a faulty CFTR allows the binding of *Pseudomonas Aeruginosa* to airway epithelium without initiation of the immune response [22].

The *P.Aeruginosa* bacterium is the main pathogen responsible for mortality in CF patients [1] contributing to around 60-70% of infections in adult CF patients [21]. Understanding the mechanisms of this bacterium's high level of antibiotic resistance is crucial to effective treatment for CF patients.

P.Aeruginosa bacteria are not typically found in isolation but are instead found in colonies encased by a highly hydrated extracellular polymer matrix (EPS), known as a biofilm [1]. Biofilm formation is one of the factors leading to the high level of antibiotic resistance found in *P.Aeruginosa* [23]. Alginate producing *P.Aeruginosa* is uniquely associated with the lungs of CF patients [24] and the presence of the alginate polymer and Pf4 virus in the biofilm leads to the formation of LC nematic phases which encase the bac-

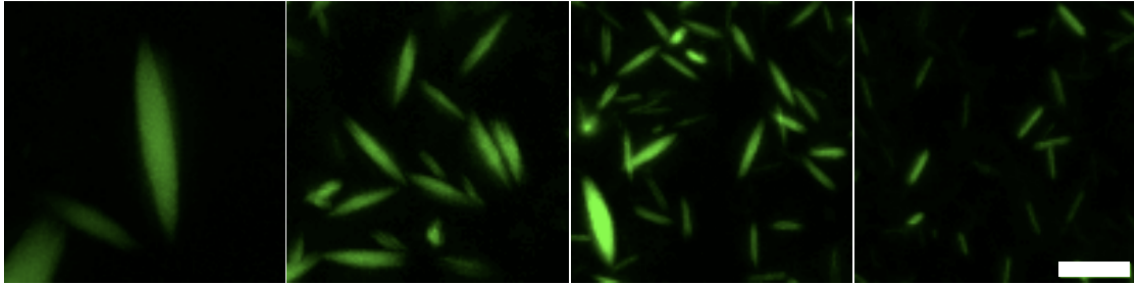


Figure 1.2: This Figure [1] are confocal microscopy images of tactoids formed from systems of Pf4 virus and sodium alginate. The scale bar is $20 \mu\text{m}$.

terium. Such LC droplets are known as tactoids. These tactoids protect the *P.Aeruginosa* and contribute to its high level of antibiotic resistance [25, 26].

The Pf4 virus found in these biofilms is a filamentous rod-like virus, which is able to form lyotropic LC [25]. In the presence of alginate polymer, the Pf4 virus experiences a depletion interaction, promoting the formation of tactoids [27, 9]. Figure 1.2 shows the shape of a number of tactoidal systems generated by de Oliveira Silva et al [1] using sodium alginate and Pf4 virus.

One of our motivations is to investigate the formation of these tactoids formed from Pf4 virus and sodium alginate [1]. We will be doing this using molecular dynamics simulations.

1.3 Molecular Dynamics

Molecular Dynamics (MD) is a computer simulation technique used to model atomic and molecular systems. This involves solving discretized equations of motion while evolving the system in time and periodically calculating properties of interest of the system. For an introduction to MD, see [28] and [29]. As outlined in [29], MD is a highly versatile tool used to measure transport properties, equilibrium and non-equilibrium properties of systems. MD is in essence a computational laboratory experiment. A indication of the similarities of MD and experimentation are shown below.

1. Setup the system of study. *Setup the experimental conditions and apparatus.*
2. Determine what variables and components we want to control. *Determine which variables of the experiment to fix and which we will allow to vary.*
3. Decide what variables in the system we wish to monitor. *Decide which observables*

in the experiment to measure and monitor.

4. Run the system and measure over time. *start the experiment and periodically record the results.*

MD allows us to investigate molecular systems without the need of approximate theories allowing us to calculate effectively exact results [29]. This provides a better comparison to experimentation than theory as it does not rely on the same approximations as theory. It also allows us to probe systems to a greater extent than experimentation as we can fine tune interactions between particles and setup systems far more readily than a typical experiment. The per particle resolution of MD allows us to investigate the behaviour of experimental systems and also validate theory [29].

MD has been applied to depletion interaction of spheres-polymer mixtures [30] and has also been applied to repulsive rigid spherocylinders [31] and repulsive semi-flexible rods and attractive tipped rods [32, 33]. This research provides us with a good baseline for our simulations to build from and to compare with. Very little investigation has been done on systems of rods + depletants [2] and LC tactoids using MD.

1.4 Scope and Outline of this Thesis

The primary motivation of this work was to investigate experimental phase behaviour of rod-like colloids in the presence of the depletion interaction. With the end goal of understanding tactoid formation in systems of Pf4 virus and sodium alginate, such as those found in CF patients. Another aim of this thesis was to compare MD to theory and prior simulation work [2].

Beginning with Chapter 2, we discuss the foundations of MD and the software package LAMMPS. We then discuss the theory on the isotropic-nematic coexistence condition in systems of rod-like colloids and polymer depletant. This will later be used as a point of comparison with MD. In Chapter 3, we discuss the implementation of MD and the modelling of rods and cells to investigate rod-like colloid + depletant phase behaviour and the formation of tactoids. In Chapter 4, we discuss the theoretical isotropic-nematic phase diagram and the results from MD simulations of attractive rods, making comparisons between the two. Subsequently, we compare our MD with the experimental work

of de Oliveira Silva et al [1]. We then discuss the *in situ* formation of tactoids in MD and compare these to experimentally observed tactoids [1]. Finally concluding with a brief summary of this thesis and discussions of avenues for further research in this field.

Chapter 2

Theory

In this chapter, we introduce the fundamental processes involved in any MD simulation. Following this, we discuss the depletion interaction and the theory required to determine the theoretical isotropic-nematic phase diagram for systems of rod-like colloids and depletants.

2.1 Molecular Dynamics

Before applying MD to tactoids and rod-like colloids, we must first introduce the basic steps involved in MD.

2.1.1 A basic approach to MD

The three universal components of any MD simulation are: initialization, force calculation and integration of Newton's equations of motion. The key steps to any MD program are outlined below.

1. Specify the initial conditions of the simulation: particle number, particle positions, particle velocity etc and the extensive/intensive variables depending on the ensemble chosen.
2. Compute all of the forces in the system using the specified interaction potentials and under the stated constraints.
3. Integrate Newton's equations of motion to obtain the new positions and velocities for each timestep.
4. Compute and measure the thermodynamic, positional and system properties at specific intervals.

5. repeat the core loop of steps 2-4 until the program has run to a specified time.

Now that we have discussed the core loop of MD we can move on the 3 key steps of any molecular dynamics simulation.

2.1.2 MD: Initialization, Force Calculation and Integrating Newton's Equations

Before you run any simulation all the properties of the initial system must first be constructed. The structure of the initial system plays a massive role in the reliability and accuracy of the simulation. Often the setup is highly contrived, such as a fully crystalline starting configuration [32, 33], see Subsection 3.2.1. It is therefore important to ensure the simulation runs for a sufficient time, so that any contrivances become insignificant. Along with setting up the configuration of the particles, we have to setup the constraints of the simulation. This includes: boundary conditions, extensive /intensive variables, potentials etc, see Section 3.2.

After initialization we have force calculation. This is typically the most time consuming component of any MD simulation. If we assume pairwise additivity (2.1), it follows that we have to calculate the interaction of every particle with all other particles.

$$U_{\text{Tot}} = \sum_{i>j} U(r_{ij}). \quad (2.1)$$

As a consequence, the length of simulation scales with $\sim N^2$. For most systems, the attraction or repulsion is relatively short ranged, so a cutoff distance is applied to reduce simulation runtime without significant impact on equilibrium behaviour. Any force calculation consists of the following steps:

1. Determine the positions of all of the particles.
2. Calculate the distance between all particle pairs within cutoff distance.
3. Calculate the force on each particle (2.2) by every other particle within cutoff and assuming pairwise additivity.

$$\mathbf{F}_{ij} = -\nabla U_{ij} \quad (2.2)$$

This algorithm assumes Newton's 3rd law [34].

Following this, we integrate Newton's equations of motion. We have chosen to do this using the Velocity-Verlet algorithm [29] as it is both accurate and computationally less

demanding than many higher order algorithms. A brief description of this algorithm is detailed below, where h is a timestep, $\tau(t)$ is the position at time t , $\mathbf{a}(t)$ is the acceleration at time t and $\mathbf{v}(t)$ is the velocity at time t .

1. Calculate $\tau(t + h)$ using $\tau(t)$, $\mathbf{v}(t)$ and $\mathbf{a}(t)$.
2. Calculate $\mathbf{a}(t + h)$ using $\tau(t + h)$.
3. Use $\mathbf{a}(t)$ and $\mathbf{a}(t + h)$ to compute $\mathbf{v}(t + h)$.

For further details see Appendix A and [29]. Now that we have discussed the basics of MD, we can discuss Langevin Dynamics (LD) a specific type of MD that was used throughout our simulations.

2.1.3 Langevin Dynamics and the Canonical Ensemble

Langevin dynamic simulations are an extension of the classic MD approach. In MD, the conservative force calculated using the inter-particle potentials, Subsection 2.1.2, is the only force to consider on each particle. In LD, we consider a simulation with two extra forces on each particle [35]: a frictional force and a stochastic thermal force. Langevin dynamic's relies on two basic assumptions:

- Stokes' law for frictional force exerting on a body moving in a liquid.
- The equipartition theorem of thermal energy [36].

The total force on a particle, i , in LD can be expressed as

$$\mathbf{F}_{\text{Tot}, i} = \mathbf{F}_{c, i} + \mathbf{F}_{f, i} + \mathbf{f}_i(t), \quad (2.3)$$

where $\mathbf{F}_{c, i}$ is the classic conservative force, $\mathbf{F}_{f, i}$ is the frictional force, t is time and $\mathbf{f}(t)$ is the stochastic thermal force. These forces can be used to craft the Langevin equation of motion [35, 37]

$$m \frac{d\mathbf{v}(t)}{dt} = \mathbf{F}_c + \mathbf{f}(t) - \xi \mathbf{v}(t) \quad (2.4)$$

with \mathbf{v} as the instantaneous velocity and ξ the friction coefficient. The friction coefficient is described by Stokes' law [38]

$$\xi = 6\pi\eta r, \quad (2.5)$$

where all the symbols have their usual meaning. $\mathbf{f}(t)$ is a rapidly fluctuating random force arising from the continuous collisions of our rods with solvent. While $\mathbf{f}(t)$ is random,

$\langle \mathbf{f}(t) \rangle = 0$. This force is the origin of Brownian motion [39]. The key utility of the Langevin method is to simulate the presence of an implicit solvent without the need to code in explicit solvent molecules, which is computationally demanding. We will discuss this implementation in subsection 3.2.2.

Langevin Dynamics is performed under the Canonical ensemble, which considers an ensemble of N systems with each system, replicating the system of interest on the thermodynamic level, consisting of a fixed volume and number of particles that is connected with a infinitely large heat bath at temperature T [40]. The heat bath is considered large enough to fulfil the limit $N \rightarrow \infty$. For a selected system in the ensemble, the other $N - 1$ systems act as the heat bath. The energy of each system can vary but the summation energy of the total ensemble is unchanged. The number of particles in each system is constant and only heat is able to flow in and out of each system to the other systems of the ensemble [40]. Now we have discussed the basics of MD and specifics of LD, we can discuss our chosen MD simulation package.

2.1.4 LAMMPS

LAMMPS stands for Large-scale Atomic/Molecular Massively Parallel Simulator [41, 42, 43]: it is a classical MD simulator, chosen because of its versatility and simplicity when compared to other MD programs. LAMMPS is capable of running simulations on a single processor or in parallel on CPUs or GPUs. When run in parallel, LAMMPS uses spatial decomposition with a message passing interface (MPI) to partition the simulation domain into subdomains with equal computational cost. These processors then communicate to one another using "ghost" atoms on the borders on the subdomains. To keep track of particles LAMMPS uses neighbor lists (NL), to determine which particles are near one another. LAMMPS is designed to model a range of potentials and atom types (atom styles), under different boundary conditions and constraints. The implementation of LAMMPS to simulate our system is detailed in Section 3.2. For a history of LAMMPS, see [43].

2.2 Phase behaviour of Rods and Depletant

2.2.1 The Depletion Interaction

In order to effectively model our rod-like colloid + depletant systems, Subsection 3.1.3, we must first discuss the characteristics and origin of the depletion interaction. The depletion interaction was first described by Asakura & Oosawa in 1954 [14] treating the polymer as hard spheres. In their seminal work, they discussed the effect of a solution of macromolecules on two immersed solid bodies. The net effect of two plates in a solution of rigid spherical macromolecules is an attraction between the two plates as a consequence of the osmotic pressure caused by the macromolecular solution. The depletion interaction was later treated using the penetrable hard sphere model [44]. The penetrable hard sphere model [44, 45] for polymer has the polymer behave like a hard sphere with rods/colloids but freely overlaps with other polymer. The pair potentials for this system are expressed as

$$U_{rr}(x) = \begin{cases} \infty, & \text{if } x < \sigma_s \\ 0, & \text{if } x \geq \sigma_s, \end{cases} \quad (2.6)$$

$$U_{dd}(x) = 0, \quad (2.7)$$

$$U_{rd}(x) = \begin{cases} \infty, & \text{if } x < \sigma_{rd} \\ 0, & \text{if } x \geq \sigma_{rd}, \end{cases} \quad (2.8)$$

where x is separation distance, hard rod is denoted by r and the polymer depletant is denoted by d . σ_r and σ_d represent the diameters of the rod and polymer respectively and $\sigma_{rd} = \frac{\sigma_r + \sigma_d}{2}$. As a result of the hard sphere interaction between depletant and rod, the depletion thickness is $\frac{\sigma_d}{2}$.

A full treatment of rod systems would require us to consider all possible orientations of the rods; however this type of directional potential is challenging to implement in MD and the primary drive of phase behaviour is based around the parallel rod configuration. We will therefore consider the depletion interaction in this case for parallel rods only.

If we consider a system of two rods in a sea of polymer, when the separation distance is less than $\sigma_r + \sigma_d$, there is a concentration gradient of polymer between the inside of the depletion zone vs bulk liquid. This results in the osmotic pressure inside the depletion

zone that is less than the bulk osmotic pressure. In bulk, the pressure applied obeys the Van't Hoff law

$$P_{\text{bulk}} = n_d k_b T. \quad (2.9)$$

where n_d is the bulk number density of depletant and the other variables take their usual meaning. It can be shown that the interaction potential, $U(x)$, with penetrable hard spheres is expressed as [9]

$$U(x) = \begin{cases} \infty, & \text{if } x < \sigma_r \\ -n_d k_b T V_{\text{overlap}}(x), & \text{if } \sigma_r \leq x \leq 2\sigma_{rd} \\ 0, & \text{if } x > 2\sigma_{rd}. \end{cases} \quad (2.10)$$

Here, $V_{\text{overlap}}(x)$ is the overlap volume of the depletion zones of parallel spherocylinders. For a spherocylinder, $V_{\text{overlap}}(x) = V_{\text{cylinder}}(x) + V_{\text{sphere}}(x)$. Where $V_{\text{cylinder}}(x)$ is the volume of overlap of two parallel cylinders, Appendix B, while $V_{\text{sphere}}(x)$, is the volume of overlap of two spherical caps, see [9] and L is the length of the cylindrical part of the rod. $V_{\text{cylinder}}(x)$ is expressed as

$$V_{\text{cylinder}}(x) = L\sigma_{rd}^2 \left[2\arccos\left(\frac{x}{2\sigma_{rd}}\right) - \sin\left(2\arccos\left(\frac{x}{2\sigma_{rd}}\right)\right) \right]. \quad (2.11)$$

While $V_{\text{sphere}}(r)$ is expressed as

$$V_{\text{sphere}}(x) = \frac{4\pi}{3}\sigma_{rd}^3 \left[1 - \frac{3}{4}\frac{x}{\sigma_{rd}} + \frac{1}{16}\left(\frac{x}{\sigma_{rd}}\right)^3 \right] \quad (2.12)$$

The overall interaction potential is obtained by combining (2.11) and (2.12) into (2.9) giving

$$U(x) = \begin{cases} \infty, & \text{if } x < \sigma_r \\ -n_d k_b T \left(L\sigma_{rd}^2 \left[2\arccos\left(\frac{x}{2\sigma_{rd}}\right) - \sin\left(2\arccos\left(\frac{x}{2\sigma_{rd}}\right)\right) \right] + \frac{4\pi}{3}\sigma_{rd}^3 \left[1 - \frac{3}{4}\frac{x}{\sigma_{rd}} + \frac{1}{16}\left(\frac{x}{\sigma_{rd}}\right)^3 \right] \right), & \text{if } \sigma_r \leq x \leq 2\sigma_{rd} \\ 0, & \text{if } x > 2\sigma_{rd}. \end{cases} \quad (2.13)$$

This result will later be used to determine the interaction potential between the rods in our simulations, subsection 3.1.3. We can now move onto a discussion of the theory required

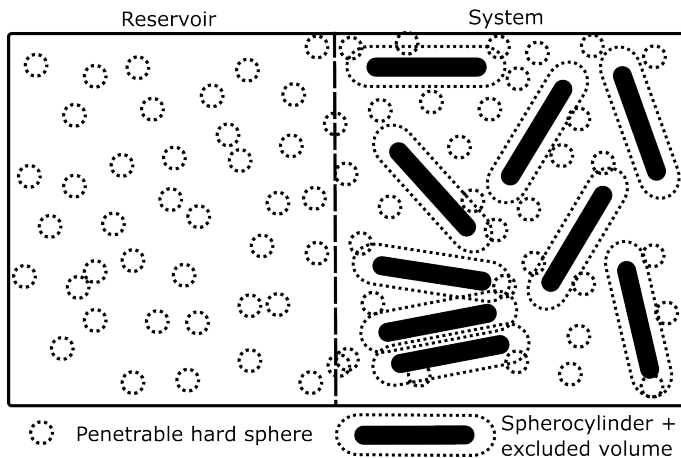


Figure 2.1: This Figure illustrates the FVT setup, here we consider a system of penetrable hard sphere polymers and rod-like colloids attached to a reservoir of polymers through a semi-permeable membrane, that only the penetrable hard sphere polymer can move between.

to map out the isotropic-nematic phase diagram. This theory was used to make predictions about MD and as a point of comparison with MD.

2.2.2 Free Volume Theory

There are several approaches that can be used to calculate the phase diagrams of systems governed by the depletion interaction [9]. The first treatment of these systems was done using thermodynamic perturbation theory (TPT) [46], where this perturbation is performed on the classic hard sphere approach [47]. This approach manifests in the formation of colloidal gas, liquid and solid phases, however, it does not account for the depletion partitioning over the coexisting phases.

Later the so called Free Volume Theory (FVT) approach was used [9, 48, 49]. Here we will cover a FVT general approach for colloids + penetrable hard sphere. The system we are considering is based on an osmotic equilibrium between colloidal rods + polymer (penetrable hard sphere) depletants, see Figure 2.1 for a visual description. Figure 2.1 consists of the FVT system, which is a system of spherocylinders + penetrable hard spheres in equilibrium with a connected reservoir of polymer with a semi-permeable membrane which allows only polymer diffusion across it. Unlike the TPT approach, FVT is not pairwise additive as it considers multiple overlaps of depletion layers which leads to a widening of the liquid phase window and is more accurate.

The starting point of FVT [9] is the calculation of the Semi-Grand Potential, $\hat{\Omega}$, de-

scribing a system of N_r rod-like colloids and N_d polymer depletants, as depicted in Figure 2.1

$$\hat{\Omega}(N_r, V, T, \mu_d) = F(N_r, N_d, V, T) - \mu_d N_d. \quad (2.14)$$

Using the thermodynamic relation

$$\left(\frac{\partial \hat{\Omega}}{\partial \mu_d} \right)_{N_r, V, T} = -N_d. \quad (2.15)$$

We can write,

$$\hat{\Omega}(N_r, V, T, \mu_d) = F_{N_d=0}(N_r, V, T) - \int_{-\infty}^{\mu_d} N_d(\mu_d') d\mu_d'. \quad (2.16)$$

$F_{N_d=0}(N_r, V, T)$ is the free energy of the colloidal particles without depletant, μ_d is the chemical potential of the depletant. The next step is deriving a function for the number of depletants in the colloid + depletant system as a function of the chemical potential imposed by the depletants in the reservoir. For the N_d calculation, we use Widom's insertion theorem [50] to obtain

$$\mu_d = \text{constant} + k_b T \ln \frac{N_d}{\langle V_{\text{free}} \rangle}. \quad (2.17)$$

$\langle V_{\text{free}} \rangle$ is the ensemble averaged free volume for the depletants in the system of hard rods.

Furthermore,

$$\mu_d = \text{constant} + k_b T \ln(n_d^R). \quad (2.18)$$

n_d^R is the number density of depletants in the reservoir, where

$$N_d = n_d^R \langle V_{\text{free}} \rangle. \quad (2.19)$$

The $\langle V_{\text{free}} \rangle$ depends on the volume fraction of the hard rods in the system and the chemical potential of the depletants. The key approximation we now make is that $\langle V_{\text{free}} \rangle = \langle V_{\text{free}} \rangle_0$. Where $\langle V_{\text{free}} \rangle_0$ is the free volume in a pure dispersion of rods. Combining this approximation with (2.19) gives

$$N_d = n_d^R \langle V_{\text{free}} \rangle_0. \quad (2.20)$$

Substituting (2.20) into (2.16) gives

$$\hat{\Omega}(N_r, V, T, \mu_d) = F_{N_d=0}(N_r, V, T) - \int_{-\infty}^{\mu_d} n_d^R \langle V_{\text{free}} \rangle_0 d\mu_d'. \quad (2.21)$$

Using the Gibbs-Duhem relation: $n_d^R d\mu_d = dP^R$ & $P^R = n_d k_b T$ then adjusting the integration limits: $\mu_d \rightarrow P_R$ & $-\infty \rightarrow 0$ gives

$$\hat{\Omega}(N_r, V, T, \mu_d) = F_{N_d=0}(N_r, V, T) - \int_0^{P^R} \langle V_{\text{free}} \rangle_0 dP^R. \quad (2.22)$$

Subsequent integration yields

$$\hat{\Omega}(N_r, V, T, \mu_d) = F_{N_d=0}(N_r, V, T) - P^R \langle V_{\text{free}} \rangle_0. \quad (2.23)$$

Using Widom's Insertion theorem [50] we can obtain the depletant chemical potential at low concentration

$$\mu_d = \text{constant} + k_b T \ln \frac{N_d}{\langle V_{\text{free}} \rangle_0}. \quad (2.24)$$

This can be rewritten as

$$\mu_d = \text{constant} + k_b T \ln \frac{N_d}{V} + W, \quad (2.25)$$

where W is the reversible work for inserting the depletant into the hard rod system. Combining (2.25) and (2.24) gives

$$\alpha = \frac{\langle V_{\text{free}} \rangle_0}{V} = \exp \left(\frac{-W}{k_b T} \right). \quad (2.26)$$

In the subsequent sections we will combine FVT with expressions for: F, W, P, μ etc, derived using a combination of Scaled Particle Theory [51] and Onsager's theory of infinitely thin hard rods [15], to solve the isotropic-nematic coexistence condition.

2.2.3 Onsager's Theory for Infinity Thin Rigid Hard Rods

Before tackling the phase behaviour of finite rigid rods with penetrable hard sphere, we first need to discuss the pioneering work of Onsager [15] on the isotropic-nematic transition in rod-like dispersions as this will provide the foundations on which subsequent theory is derived.

The proceeding theory follows a similar structure to [9]. Onsager's second virial theory makes the assumption of infinity thin rigid hard rods, thus $L/D \rightarrow \infty$, where L is rod

length and D is rod diameter. In this system, the excluded volume and regular volume of the rods ignore the spherical caps, essentially assuming a purely cylindrical rod. The Helmholtz free energy for a dispersion of N rigid hard rods in volume V in the second virial approximation is expressed as [52]

$$\frac{F[f]}{NkT} = \text{constant} - 1 + \ln(c) + \sigma[f] + c\rho[f], \quad (2.27)$$

where f is the orientational distribution function and we have lumped all constants into one term. c is the dimensionless concentration, expressed as

$$c = bn = B_2\rho = \frac{L}{D}\phi, \quad (2.28)$$

where $n = N/V$ is the number density of the rods and $b = (\pi/4)L^2D$ is the excluded volume of an infinitely thin rigid rod and B_2 is the second virial coefficient for the virial expansion of pressure of an imperfect gas [53]. The volume fraction (ϕ) is expressed as

$$\phi = \nu_0 n, \quad (2.29)$$

where $\nu_0 = (\pi/4)D^2L$ is the volume of the rod. $\sigma[f]$ is the per particle orientational entropy. The orientational entropy is expressed as

$$S_{\text{or}} = -Nk \int f(\omega) \ln[4\pi f(\omega)] d\omega \equiv -Nk\sigma[f]. \quad (2.30)$$

$f(\omega)$ is the orientational distribution function which expresses the probability of finding a spherocylinder with an orientation characterized by solid angle, ω . This orientational distribution function must be normalized

$$\int f(\omega) d\omega = 1. \quad (2.31)$$

In the isotropic case, all orientations are equally probable which implies

$$f_{\text{iso}}(\omega) = \frac{1}{4\pi}. \quad (2.32)$$

This is in accordance with the prior normalization of $f(\omega)$. The final term $-kc\rho[f]$ is the packing entropy per particle. $\rho[f]$ is

$$\rho[f] = \frac{1}{4\pi} \iint |\sin(\theta)| f(\omega) f(\omega') d\omega d\omega', \quad (2.33)$$

Solution Method	c_I	c_N	S_2
Numerical Method	3.290	4.191	0.7922
Onsager's Trial Function	3.290	4.191	0.848
Gaussian Trial Function	3.451	5.122	0.910

Table 2.1: This Table compares the output coexistence concentrations and S_2 values for solving the coexistence condition using numerical methods, Onsager's trial function and Odijk's Gaussian trial function. S_2 is the nematic order parameter, see Section 3.3.1.

where θ is the angle between the rods which depends on the orientations ω and ω' . The orientational and packing entropy for the isotropic phase are expressed as

$$\sigma_I = 0, \rho_I = 1. \quad (2.34)$$

These values make sense as the isotropic phase has no orientational or packing order.

The nature of the isotropic-nematic transition derives from the competition of the orientational entropy vs the packing entropy. Low concentration systems favour the orientational entropy which is maximised for the isotropic phase. However, for high concentration systems the packing entropy becomes more dominant thus favouring the nematic phase. For intermediate concentrations, it is common to observe a coexistence of the isotropic and nematic phase, which maximises the orientational entropy in the isotropic phase and the packing entropy in the nematic phase.

For coexistence of isotropic and nematic phase, both phases must be in mechanical and chemical equilibrium with one another

$$P_I(c_I) = P_N(c_N), \quad (2.35)$$

$$\mu_I(c_I) = \mu_N(c_N). \quad (2.36)$$

Solving the coexistence condition can be done numerically or by using a trial orientational function with variational parameters that are minimized wrt Helmholtz free energy. Table 2.1 compares the numerical solution method to Onsager's trial function [15] and Odijk Gaussian trial function [54, 55]. For all three methods F_I is expressed as

$$\frac{F_I[f]}{Nk_b T} = \text{constant} - 1 + \ln(c) + c. \quad (2.37)$$

Using standard thermodynamic relations

$$P = -\frac{\partial F}{\partial V}, \mu = \frac{\partial F}{\partial N}. \quad (2.38)$$

we obtain

$$\frac{P_I b}{kT} = c_I + c_I^2, \quad (2.39)$$

$$\frac{\mu_I b}{kT} = \text{constant} + \ln c_I + 2c_I. \quad (2.40)$$

where b is the excluded volume of an infinitely thin rod, I and N denote the isotropic and nematic phase respectively.

Odijk first proposed the Gaussian trial function [54, 55] in 1985. This provides an accurate and easy way to solve the coexistence condition. We will proceed with this method in subsequent systems. For a summary of all approaches, see [9]. For details of the numerical method, see [56, 57, 58, 59] and for details on trial functions, see [48]. The Gaussian trial function is expressed as

$$\begin{aligned} f_G &\sim \tilde{N}(\kappa) \exp\left(\frac{1}{2}\kappa\theta^2\right), 0 \leq \theta \leq \frac{\pi}{2}, \\ &\sim \tilde{N}(\kappa) \exp\left(\frac{1}{2}\kappa(\pi-\theta)^2\right), \frac{\pi}{2} \leq \theta \leq \pi, \end{aligned} \quad (2.41)$$

where κ is a variational minimization constant, θ is the angle between two rods and $\tilde{N}(\kappa)$ is the normalization constant. The advantage of the Gaussian representation is that σ and ρ can be expressed accurately as

$$\sigma[f_G] \sim \ln(\kappa) - 1 \quad (2.42)$$

and

$$\rho[f_G] \sim \frac{4}{\sqrt{\pi\kappa}}. \quad (2.43)$$

This gives the following Helmholtz free energy expression for the nematic phase

$$\frac{F_N}{Nk_b T} = \text{constant} - 1 + \ln c + \ln \kappa - 1 + \frac{4c}{\sqrt{\pi\kappa}}, \quad (2.44)$$

and minimizing this wrt κ yields

$$\kappa = \frac{4c^2}{\pi}. \quad (2.45)$$

F_N is therefore expressed as

$$\frac{F_N}{Nk_b T} = \text{constant} + \ln \frac{4}{\pi} + 3\ln c. \quad (2.46)$$

Using the relations (2.38) we obtain P_N and μ_N

$$\frac{P_N b}{k_b T} = 3c_N \quad (2.47)$$

$$\frac{\mu_N}{k_b T} = \text{constant} + \ln \frac{4}{\pi} + 3 + 3\ln c_N. \quad (2.48)$$

As we have solved the coexistence condition in the limit of infinitely thin rigid rods, we now proceed to solve the coexistence condition for finite rods.

Solving the Isotropic-Nematic Coexistence Condition for Finite Rods

To solve the coexistence condition for finite rods, we use Scaled Particle Theory [51] to determine the reversible work of insertion of a finite spherocylinder into a suspension of spherocylinders, Appendix C. When we solve the coexistence condition for finite rods, using the Gaussian method, we obtain a new expression for the variational minimization constant κ

$$\kappa = \frac{36}{\pi} \frac{(\gamma - 1)^4}{(3\gamma - 1)^2} \left(y + \frac{2\gamma}{3\gamma - 1} y^2 \right)^2. \quad (2.49)$$

where $y = \frac{\phi}{1-\phi}$, where ϕ is the volume fraction of the rods and $\gamma = 1 + \frac{L}{D}$. Along with this we obtain the, Helmholtz free energy, chemical potential and pressure for the pure finite sized rod systems, see Table 2.2. Now that we have covered the pure system of finite rods, we can move on to discussing a system of finite rods with penetrable hard sphere polymer present. As we have obtained the necessary expressions for: F , P , μ and κ for our finite rod system, we can now consider systems of Finite Rigid Rods + penetrable hard spheres.

2.2.4 The Phase Behaviour of Finite Rigid Rods with Penetrable Hard Spheres

In the finite rod + penetrable hard sphere system, the attractive depletion interaction means that B_2 no longer dominates the virial expansion and B_3 now has to be considered [60]. This means that we must start from a theory that takes into account the higher order virial coefficients. We are going to again use SPT [51] to do this but instead considering the insertion of a penetrable hard sphere into a system of finite sized rods.

Variable	expression
$\frac{F[f]}{Nk_b T}$	constant' - 1 + $\sigma[f] + \ln y + A[f]y + \frac{1}{2}B[f]y^2$
$\frac{\mu}{k_b T}$	constant + $\ln y + \sigma[f] + (1 + 2A[f])y + \left(A[f] + \frac{3}{2}B[f]\right)y^2 + B[f]y^3$
$\frac{P\nu_0}{k_b T}$	$y + A[f]y^2 + B[f]y^3$
$A[f]$	$3 + \frac{3(\gamma - 1)^2}{(3\gamma - 1)}\rho[f]$
$B[f]$	$\frac{12\gamma(2\gamma - 1)}{(3\gamma - 1)^2} + \frac{12\gamma(2\gamma - 1)^2}{(3\gamma - 1)^2}\rho[f]$
ν_0	$\frac{\pi}{4}LD^2 + \frac{\pi}{6}D^3$

Table 2.2: This Table summarises the important equations from the SPT of finite rods, Appendix C.

The starting point of this calculation of phase behaviour is the Semi-Grand Potential [61, 62] for a system of rods + penetrable hard sphere in osmotic equilibrium with the reservoir of penetrable hard sphere as found in Subsection 2.2.2 on FVT. The Semi-Grand Potential is expressed as (2.23) where $F(N_r, V, T)$ is described using the SPT expression in Table 2.2, $P^R = n_d^R k_b T$. n_d^R is the number density of the penetrable hard sphere in the reservoir. The free volume is expressed as (2.26). Where W in (2.26) is the reversible work of inserting a penetrable hard sphere into a hard rod suspension found in (2.23). The work is calculated by expanding the penetrable hard sphere from a diameter of 0 to its final diameter, σ_d . The scaled penetrable hard sphere has a diameter of $\lambda\sigma_d$, where λ is the scaling parameter. In the limit of $\lambda \rightarrow 0$, the inserted penetrable hard sphere is a point particle. In this case, it is very unlikely that the excluded volume of the hard rods and scaled penetrable hard sphere will overlap. So

$$W(\lambda) = -k_b T \ln[1 - n_r \nu_{\text{excl}}(\lambda)], \text{ for } \lambda \rightarrow 0, \quad (2.50)$$

where n_r is the number density of rods $\nu_{\text{excl}}(\lambda)$ is the excluded volume of the added scaled penetrable hard sphere and a hard spherocylinder with length L and diameter D

$$\nu_{\text{excl}}(\lambda) = \frac{\pi}{4}(D + \lambda\sigma)^2 L + \frac{\pi}{6}(D + \lambda\sigma)^3. \quad (2.51)$$

coefficient	expression
a	$\frac{6\gamma}{3\gamma-1}q + \frac{3(\gamma+1)}{3\gamma-1}q^2 + \frac{2}{3\gamma-1}q^3$
b	$\frac{1}{2} \left(\frac{6\gamma}{3\gamma-1} \right)^2 q^2 + \left(\frac{6}{3\gamma-1} + \frac{6(\gamma-1)^2}{(3\gamma-1)^2} \rho[f] \right) q^3$
c	$\frac{2}{3\gamma-1} \left(\frac{12\gamma(2\gamma-1)}{(3\gamma-1)^2} + \frac{12\gamma(\gamma-1)^2}{(3\gamma-1)^2} \rho[f] \right) q^3$

Table 2.3: This Table gives the meaning of a , b and c in (2.56).

In the limit of $\lambda \gg 1$, the phs depletant is very large and it will almost certainly overlap with multiple excluded volumes. The W required is equal to the volume work to create a cavity. The cavity volume is $\frac{\pi}{6}(\lambda\sigma)^3$. Using the classic expression for work, $W = PV$, we obtain

$$W = \frac{\pi}{6}(\lambda\sigma)^3 P, \text{ for } \lambda \gg 1. \quad (2.52)$$

Here P is the osmotic pressure of a system of hard rods as given in Table 2.2. In SPT, we can combine the two limiting cases by expanding W in a Taylor series of λ ,

$$W(\lambda) = W(0) + \left(\frac{\partial W}{\partial \lambda} \right)_{\lambda=0} \lambda + \frac{1}{2} \left(\frac{\partial^2 W}{\partial \lambda^2} \right)_{\lambda=0} \lambda^2 + \frac{\pi}{6}(\lambda\sigma)^3 P. \quad (2.53)$$

In the $\lambda = 1$ case

$$\frac{W(\lambda = 1)}{k_b T} = \ln(1 - \phi_r) + \left[\frac{6\gamma q}{3\gamma - 1} + \frac{3(\gamma + 1)q^2}{(3\gamma - 1)} \right] y_r + \frac{1}{2} \left(\frac{6\gamma}{3\gamma - 1} \right)^2 q^2 y_r^2 + \frac{2q^3}{3\gamma - 1} \frac{P\nu_0}{k_b T}, \quad (2.54)$$

where $y_r = \frac{\phi_r}{1 - \phi_r}$, $\gamma = 1 + \frac{L}{D}$ and $q = \frac{\sigma_d}{D}$. Inserting the P and ν_0 from Table 2.2 into (2.54) and inserting this into (2.26 leads to the following expression for α

$$\alpha = (1 - \phi_r) \exp(-Q(\phi_r)) \quad (2.55)$$

where,

$$Q(\phi_r) = ay_r + by_r^2 + cy_r^3 \quad (2.56)$$

where a , b and c are found in Table 2.3.

In the limit of $L = 0$ and $\gamma = 1$, α will correspond to the result for spherical colloids and penetrable hard sphere depletant.

Using FVT and SPT, we can now construct the phase diagram for the system of interest using the following steps:

1. Define the system variable values: L , D , R_g , see Table 4.1. These are determined in Chapter 3.
2. Define κ , $\rho[f]$ and $\sigma[f]$ for the nematic system, determined from the Gaussian solution of the isotropic-nematic transition from Table 2.2.
3. Calculate the pressure and chemical potential for the pure isotropic and nematic systems using the equations in Table 2.2.
4. Combining the pure results and (2.57) and (2.58) with equations: (2.55), (2.56) and Table 2.3, calculate the pressure and chemical potential for the isotropic and nematic phases with depletants, using

$$P = - \left(\frac{\partial \hat{\Omega}}{\partial V} \right)_{N_R, \mu_d} = P^0 + P^R \left(\alpha - n_r \frac{d\alpha}{dn_r} \right)_{V, \mu_d} \quad (2.57)$$

and

$$\mu = \left(\frac{\partial \hat{\Omega}}{\partial N_r} \right) = \mu_r^0 - P^R \frac{d\alpha}{dn_r} \quad (2.58)$$

5. Solve the isotropic-nematic coexistence conditions by equating the chemical potentials and pressures as seen in (2.35) and (2.36) for multiple ϕ_d values.

The resulting isotropic-nematic phase diagram is shown and discussed in Section 4.1.

We have only considered the isotropic-nematic coexistence as our theory is not the central focus of this work. The theory is used as a starting point on which to predict and compare with the results of our MD. MD will be used to probe higher order phases such as smectic C and crystalline.

Chapter 3

Modelling and Simulations

In this chapter, we outline the methods used to model rods, cells and the depletion interaction. We then discuss the use of LAMMPS and MD to simulate systems of attractive rods & cells.

3.1 System Modelling

In the previous chapter, we discussed the basics of MD, Section 2.1. We will now tackle the specifics of MD including our model for PF4 virus (rods) and *P.Aeruginosa* (cell), how we simulate the depletion interaction and the implementation in LAMMPS.

3.1.1 Modelling of Rigid Rods

The Pf4 virus is a rigid poly-disperse filamentous virus rod [1] with a very large L/D ratio, see Table 3.1. For simplicity, we will be modelling all rods as infinitely rigid. The high level of polydispersity in Pf4 virus [1] is ignored and we will use monodisperse rods. Systems containing Pf4 virus have a composition of $\sim 35\%$ so called "ghost" virus. The "ghost" virus, is also filamentous but does not contain RNA, and is therefore significantly less massive than the "non-ghost" Pf4 rods and is on average shorter than the Pf4 virus [1]. The weighted average mass of the ghost and Pf4 is found in [1]. We will be ignoring the presence of ghost virus in our MD.

LAMMPS has a number of options that could be used to simulate rigid rods, many of which were tested. As you cannot model solid bodies in LAMMPS with traditional pair potentials, the most appropriate model involved using overlapping spheres to model a "smooth" rod. Figure 3.1, I and II illustrate the rods being modelled as a series of either

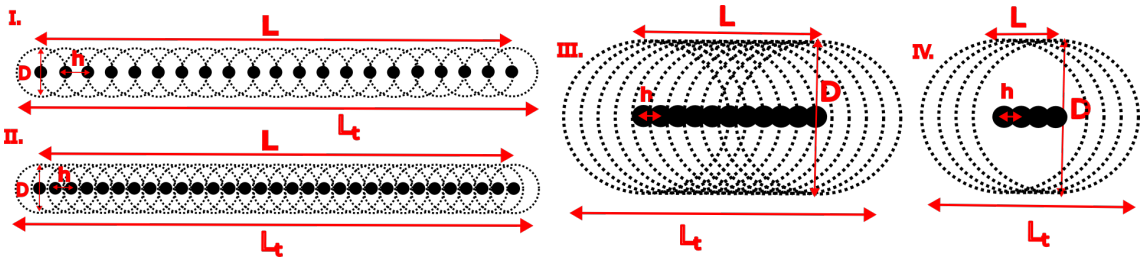


Figure 3.1: This Figure shows the model for the Pf4 virus and *P.Aeruginosa*. I is the 21 particle rod, II is the 31 particle rod, III is the 11 particle long cell and IV is the 4 particle short cell. L = Cylinder length, L_t = Total length, D = Diameter and h = separator distance. See Table 3.1 for dimensions and properties of I-IV.

21 or 31 overlapping spheres. To model this system, we use atom_style bond within LAMMPS, each atom with this style is assigned: an atom_ID, a molecular_ID, a mass and an initial 3D position. All atoms with the same molecular_ID are fixed and non-interacting relative to one another. All atoms are point masses with repulsive radii defined by the diameter of the rod, D . Spheres within the same rod have partial overlap with one another leading to the formation of a "smoother" rod, preventing any strange effects such as rods intersecting/crossing each other. This overlap further leads to a more adequate fitting of the LJ potential to the DI, see Subsection 3.1.3. The main issue with this approach is the L/D ratio of the rods. To mimic the Pf4 exactly would require each rod to contain at a minimum 1000 particles, this is too computationally demanding, so we use a smaller L/D . The L/D ratio has been scaled from Pf4's value of 428 to 9 for our system. The length and mass are somewhat arbitrary here, but are implemented consistently in order to compare with the FVT phase diagram, subsection 4.1.1 and observe the formation of tactoids, Section 4.2. The mass chosen will primarily effect the particle velocity and chosen timestep. For full details of the properties of the rods, see Table 3.1.

3.1.2 Modelling the Cell

The *P.Aeruginosa* cell can vary in length from 1-5 μm and diameter from 0.5-1 μm [63]. Similar to the rod case in Section 3.1.1 a number of approaches were considered to model the cell of our tactoid system. Due to the relatively cylindrical shape of *P.Aeruginosa*, we modelled the cell in the same way as the rods above. The difference between the two models being the different dimensions of the cells. See Figure 3.1 III and IV for an image of the cells that were used and Table 3.1 for their properties.

Name/ID	Total Length(L_t) (nm)	Cylinder Length(L) (nm)	Diameter(D) (nm)	separator(h) (nm)	$\frac{L}{D}$	mass(m) (kg)
Pf4 viral rod	3000	~ 3000	7	N/A	48	$71.1 \times 10_{-21}$
21 Particle Rod (I)	70	63	7	3.15	9	$1.661 \times 10_{-23}$
31 Particle Rod (II)	70	63	7	2.1	9	$1.661 \times 10_{-23}$
III	200	100	100	10	1	10^{-12}
VI	130	30	100	10	0.3	0.35×10^{-12}

Table 3.1: This Table shows the dimensions and properties of the cells and rods detailed in Figure 3.1. As well as the dimensions of Pf4 virus.

3.1.3 Modelling the Depletion Interactions using the Lennard-Jones Potential

A number of approaches were considered when modelling the depletion interaction. One such method was modelling explicit polymer to generate the depletion interaction *in-situ*, however, it proved to be computationally expensive and lack the utility to map the isotropic-nematic phase diagram as it is hard to generate high ϕ_r systems due to the initial volume constraints. Instead we used a Lennard-Jones potential that we fit to the depletion interaction [64, 65]. Within the fitting approach, the polymer is part of the implicit solvent and modelled through the LD method. For a comparison with the explicit polymer method, see Subsection 4.1.4 and [2]. There are two main reasons that we do not explicitly use the depletion interaction potential.

Firstly, the depletion interaction for rods is directional. The potential is dependent on the volume of overlap between two rods, $V_{\text{overlap}}(x)$, which itself depends on: rod length, rod diameter, orientation of the rods (ω, ω') and separation distance, x , see (2.13). While it is somewhat possible to account for different orientations in LAMMPS, it is challenging to implement and unnecessary to achieve adequate phase behaviour.

Secondly, we cannot use the depletion interaction directly in MD because of the hard component of the depletion interaction which is an infinite step functions meaning the interaction potential is discontinuous. This leads to forces which are discontinuous because force is calculated as $-\left(\frac{\partial U}{\partial x}\right)$. Despite the fact that we cannot use the infinite potential directly we still want to fit the depletion interaction to a potential with steep continuous repulsion at rod contact. The LJ potential was chosen because it consists of a superposition of a smooth attractive tail and steep repulsion at short distances.

The phase behaviour of rods is primarily driven by two factors; the repulsion between

rods at close distance and the depletion interaction for rods in a parallel configuration. We therefore decide to fit the LJ potential to the depletion interaction for two parallel rods (2.13), subsection 2.2.1. The LJ potential takes the form

$$U_{\text{LJ}}(x, \sigma, \epsilon) = 4\epsilon \left[\left(\frac{\sigma}{x}\right)^{12} - \left(\frac{\sigma}{x}\right)^6 \right], \quad (3.1)$$

where $U(x, \sigma, \epsilon)$ is the interaction potential, x is the separation distance, ϵ is the potential minimum and σ is the distance at which the repulsive and attractive terms cancel. The LJ potential is ideal for fitting to the depletion interaction for a number of reasons.

Firstly, the steep repulsive term can be adequately fitted to the infinite component of the depletion interaction, so phase behaviour is accurately emulated. Secondly, the LJ potential contains a smooth attractive tail, next to the strong repulsive term, this mimics the general shape of the depletion interaction and thus makes fitting of the attractive and repulsive simultaneously relatively straightforward. Thirdly, the LJ potential is practical as it is readily available in LAMMPS, easily customised to account for varying polymer concentration and gyration radii of different systems and finally, the LJ potential is omnidirectional making implementation simple.

Parallel fitting will lead to a larger LJ potential than is optimal and a longer ranged attraction than the "true" depletion interaction. As our rods are composed of multiple spheres, we are not fitting a single LJ potential to the rod depletion interaction but instead fitting the rod depletion interaction to a summation of LJ interactions, this will be referred to as the SLJ. The SLJ takes the form

$$U_{\text{total, LJ, N}}(x, \sigma, \epsilon) = N \times U_{\text{LJ}}(x, \sigma, \epsilon) + 2 \sum_{n=1}^{N-1} ((N-n) \times U_{\text{LJ}}((x^2 + (n \times h)^2)^{1/2}, \sigma, \epsilon)) \quad (3.2)$$

where $N = 21, 31$ for the 21 and 31 particle rods respectively and h is found in Table 3.1. The SLJ in both cases shows a minimum shift to the right of $\sigma = D$ and a broadening of the attractive tail and repulsive slope. To fit the depletion interaction to SLJ, an offset of $0.133R$ and $0.131R$ was applied respectively to 21 and 31 particle rods respectively, this ensures that the depletion interaction hard repulsion occurs at $r = D$. In both cases the optimal R_g is 3.31 nm. But the relation of ϵ to ϕ_d varies from the 21 to 31 particle rods.

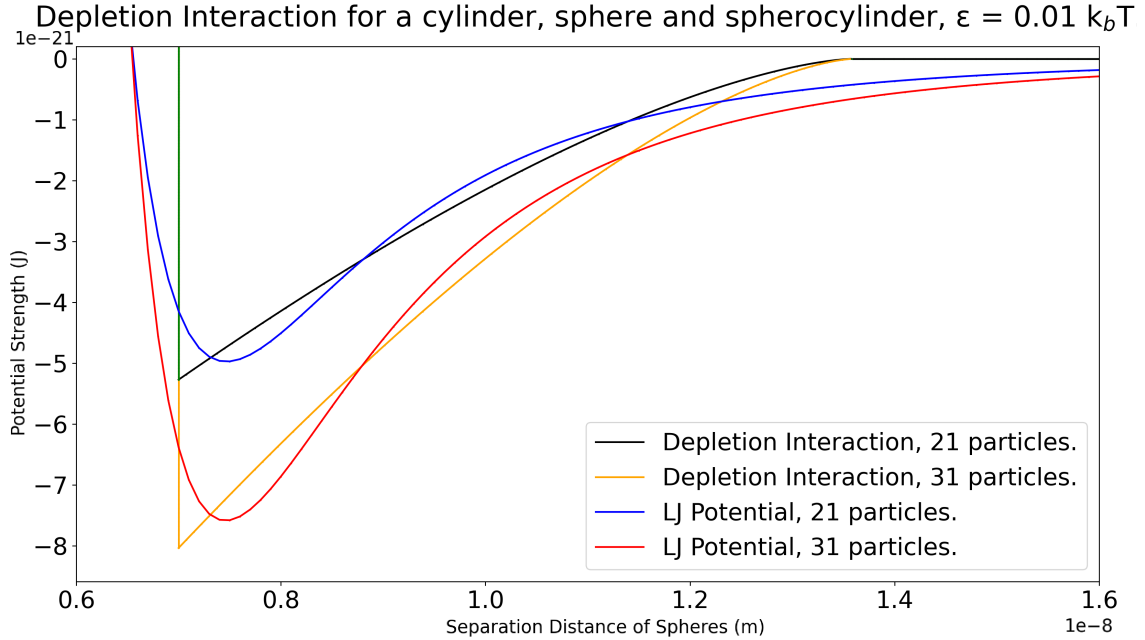


Figure 3.2: This Figure shows the fitting of the depletion interaction to the SLJ potential for the 21 and 31 particle rods, for $\epsilon = 0.01 k_b T$.

The equations relating ϕ_d to ϵ for 21 particle and 31 particle rods take the form

$$\begin{aligned} \text{SLJ(21 particles): } \phi_d &= 5.0291 \times \frac{\epsilon}{k_b T} + 1 \times 10^{-7}, \\ \text{SLJ(31 particles): } \phi_d &= 7.6412 \times \frac{\epsilon}{k_b T} - 2 \times 10^{-5}. \end{aligned} \quad (3.3)$$

Fitting was performed using Scipy [66, 67]. The polymer found in the experimental work of de Oliveira Silva et al [1] is sodium alginate, which typically has a R_g between 20 – 40nm [68]. This means that the experimental systems have a significantly longer ranged interaction than the interaction we are considering. This may lead to some differences between experimental and MD, Section 4.1.

The 21 and 31 particle rods were necessary to scan a large ϕ_d phase space. For low ϕ_d values, a 21 particle rod is insufficient to model accurate phase behaviour as the reduced steepness of the SLJ leads to non-overlapping repulsive potentials and allows the rods to intersect and cross one another.

When modelling the rods with 0 depletant ($\phi_d = 0$) we used a shifted and truncated LJ potential, known as the Weeks-Chandler-Anderson (WCA) potential, see [69]. The

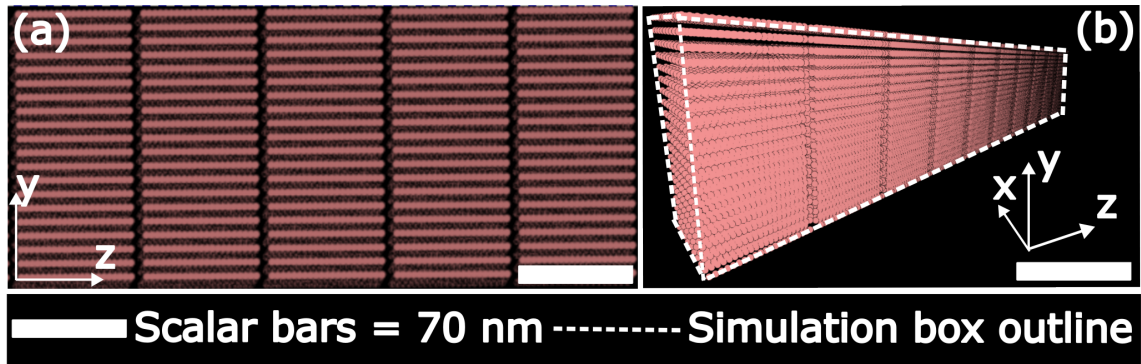


Figure 3.3: This Figure shows an example initialization system. (a) is a side on view showing the stacking of rods in the crystalline stack. (b) shows a perspective view of an initial system with the simulation box outline.

form of this potential is

$$U_{\text{WCA}}(x, \sigma, \epsilon) = \begin{cases} 4\epsilon \left[\left(\frac{\sigma}{x}\right)^{12} - \left(\frac{\sigma}{x}\right)^6 \right] + \epsilon, & \text{if } x \leq 2\frac{1}{6}\sigma_r \\ 0, & \text{if } x > \frac{1}{6}\sigma_r. \end{cases} \quad (3.4)$$

This potential is a short range repulsion, where $\sigma = D$ and ϵ which is the well depth of the LJ potential and determines the "steepness" of the repulsive potential. Without the presence of the depletion interaction the rods are just repulsive rigid rods which have already been modelled extensively [32, 33].

3.1.4 Cell Interactions

When considering systems with cells our focus is on the cell-rod interaction to form tactoids and as we only have one cell per simulation box, cell-cell interactions are ignored.

To model the cell-rod interactions we use the LJ potential (3.1). In the cell-rod case, $\sigma = R_r + R_c$ where R_r is the radius of the rod and R_c is the radius of the cell. Varying the ϵ of the cell-rod interaction is done arbitrarily, this changes the alignment of the rods around the cell and the thickness of the formed tactoid, Subsection 4.2.3. We have now discussed all the interactions and particles we are modelling, and can move on to the implementation of our simulations within LAMMPS.

3.2 LAMMPS Implementation of Molecular Dynamics

3.2.1 Initialization

Within the initialization step we have to set parameters and compute particle initial configurations and positions. The distance between all rods in the initial configuration must

be sufficient to insure there is not excessive repulsion upon starting the simulation.

Randomly generating rods in different orientations and insuring that the separation is sufficient is not only impractical to do but typically leads to unrealistic systems rather than the expected equilibrium behaviour [33]. The way to get around this is to start with the rods in a spaced crystalline style configuration, Figure 3.3. To adjust the concentration we can take the same rod configuration and expand the volume of the box in the z axis to reduce the ϕ_r in the system. All of my systems consist of either 2000 rods or 1000 rods these are automatically generated using a Python 3.11 [67] data generating script, Appendix D.

LAMMPS initialization of complicated systems typically involves the use of two setup files: the input file and the data file. The data file lists the number of atoms, atom mass, box dimensions, atom IDs, molecular IDs and atomic coordinates. The input file is the file that is run directly in the command prompt, see Appendix E for a typical input script. We import the data file into the input file. The input file contains the setup for every other aspect of the simulation not covered in the data file, this includes: unit system, boundary conditions, dimension, atom_types, potential_types, potential parameters, grouping, fixes, computation, outputs and dump files.

3.2.2 Factors to consider in the LAMMPS Input File.

Within the input file a number of parameters and conditions have to be set, some of which are described below.

Following from the work of [33], we set the timestep for our system involved with use of the LJ_timescale

$$LJ_timescale = \left(\frac{m}{k_b T} \right)^{1/2} D, \quad (3.5)$$

where m is the mass of a rod, D is the diameter of the rod. The value of the LJ_timestep for our system is $4.43 \times 10^{-10} s$. The value for the timesteps are set as $\sim 10^{-2} \times LJ_timescale$. Along with these timescales, we have to consider the equilibration of temperature in Langevin Dynamics, this is done every $100 \times$ timesteps.

Some other factors that are specified in our LAMMPS simulations are listed below

1. Prior to equilibration, we apply a cg-style minimization [70] this is used for trou-

bleshooting.

2. We use periodic boundary conditions [71, 29], this ignores possible wall effects without the computational expense of large systems.
3. Velocities are setup on a displaced Gaussian distribution. As LAMMPS does not use the Boltzmann distribution [72, 73].

All of my systems are ran under LD with implicit solvent/polymer. This requires a random seed and dampening parameter. The dampening parameter specified in timestep units determines the temperature relaxation time. This factor is inversely related to the viscosity of the solvent, so a small relaxation time implies a high viscosity solvent. The specified random seed, is required for the Marsaglia random number generator [74]. Each processor uses the input seed to generate its own unique seed and stream of random numbers. This seed generates the system "white noise". This white noise forms the random stochastic solvent force [75] and randomizes the direction and magnitude of these forces, the magnitude of this random force is proportional to $\sqrt{\frac{k_b T m}{dt \times \text{damp}}}$, where damp is dampening parameter mentioned above.

Other aspects of the initialisation include: neighbor_number, communication_distance and bin_type, these effect both system stability, efficacy and runtime. For further details see [42].

3.3 Monitoring the Simulation

After initializing the system we now need to decide what data to collect and how to interpret/visualise the data.

3.3.1 Measuring Order - Order Parameter Calculation

An order parameter is a normalized variable which measures the degree of order in a system [32, 33]. In systems of rods multiple order parameters are used for full classification of the phase behaviour. Quantitative analysis of S_2 was performed on my systems, along with a qualitative analysis of smectic order, (τ) and hexatic order (ψ_6).

S_2 measures the degree of orientation of the rods to the systems preferential director. This is the parameter I am most interested in quantifying. A true crystalline system will have full alignment along a director with $S_2 = 1$. A truly isotropic system will have no

preferential orientation, $S_2 = 0$. The global nematic order parameter can be obtained from the following tensor [33]

$$Q_{vw} = \frac{1}{N} \sum_{j=1}^N \left(S_{jv} S_{jw} - \frac{1}{3} \delta_{vw} \right), \quad (3.6)$$

where v, w corresponds to the components of the vector of the particle, \mathbf{S} , in the Cartesian coordinate system and δ_{vw} is the Kronecker delta. \mathbf{S} is defined as

$$\mathbf{S} = \sum_i \frac{\hat{\mathbf{s}}_i}{b-1}, \quad (3.7)$$

where $\hat{\mathbf{s}}_i$ represents the normalised orientation of a bond within a rod, $\hat{\mathbf{s}}_i = \mathbf{s}_i / s_i$, and $s_i = |\mathbf{s}_i|$ is the length of the bond. The variable b represents the numbers of bonds within the rod. In my case, due to the use of rigid rods the orientation of all bonds within the same rod will be identical and the value of b is 10 for all systems.

The value of S_2 and the director, $\hat{\mathbf{n}}$ is obtained as the largest eigenvalue and eigenvector of the tensor (3.6) respectively. S_2 of one configuration is proportional to the average acute angle between the director and the direction of each molecule θ .

$$S_2 = \langle P_2(\cos(\theta)) \rangle = \frac{3}{2} \langle \cos^2 \theta \rangle - \frac{1}{2}, \quad (3.8)$$

where P_2 is the second Legendre polynomial, $P_2 = (3q^2 - 1)/2$.

In order to obtain the S_2 from LAMMPS [43] we use the python package Freud-analysis [76]. This allows us to obtain the S_2 and director using quaternions directly outputted from LAMMPS. Quaternions [77] are typically represented as a 4 component vector [78]

$$\hat{\mathbf{s}} = a + b\hat{\mathbf{i}} + c\hat{\mathbf{j}} + d\hat{\mathbf{k}}. \quad (3.9)$$

Freud-analysis directly outputs the nematic tensor for the whole system. The largest eigenvalue corresponds to S_2 and its eigenvector is the director.

τ and ψ_6 are classified by eye. τ is determined by looking at the gaps between multiple organised layers of rods. ψ_6 is determined by looking at the nearest neighbor coordination environment around each rod. As the system order increases we would expect S_2 to increase first, then τ and finally ψ_6 .

3.3.2 Collecting Thermodynamic Data

Monitoring of our simulation also requires collection of the thermodynamic data. There is a plethora of thermodynamic data that can be calculated as our output by LAMMPS [43]; for more details on thermodynamic outputs, see [42]. In the case of my system, we require the following thermodynamic data: Temperature, Pressure, Kinetic Energy (KE), Potential Energy (PE), Total Energy (TE), Atom Number and Volume. Unlike some other LAMMPS thermodynamic outputs, these require very little additional computation.

The thermodynamic data in our system is used to troubleshoot errors in precursor simulations and determine if equilibrium has been established.

The temperature in Langevin/NVT simulations is computed [29, 42] from

$$KE = \frac{d}{2} N k_b T, \quad (3.10)$$

where all in the equation take their usual meaning. This assumes that the equipartition theorem is obeyed [29]. The pressure is computed as

$$P = \frac{N k_b T}{V} + \frac{1}{V d} \times \sum_{i=1}^{N'} (\mathbf{r}_i \wedge \mathbf{f}_i), \quad (3.11)$$

where N is the number of particles in the simulation, d is the dimensionality, \mathbf{r}_i and \mathbf{f}_i is the position vector and force vector of particle, i and the rest of the constants take their usual meaning. Note the second term is the virial coefficient equal to $-\frac{dU}{dV}$, this is computed pairwise for all interactions. This is computed in parallel for each subdomain and then summed over all parallel processes. Thus N' necessarily includes the ghost atoms within the summation. For a detailed account of how LAMMPS computes the virial coefficient effectively, see [79]. For many soft condensed matter systems pressure fluctuations from +ve to -ve are common due to fact that force can be attractive and repulsive. The pressure is only useful to help determine why precursor simulations may of failed.

3.3.3 Establishing Equilibrium

Determining if a system is in dynamic equilibrium can be a challenge. The KE and Temperature are not appropriate as, excluding the first 20,000 timesteps, they fluctuate around the fixed equilibrium value. The pressure is not suitable as it fluctuates from +ve to -ve

throughout the entire simulation and shows little difference from system to system.

The primary method for determining equilibrium involved watching the convergence of PE to a constant value. However, this does not confirm if the system is in the thermodynamic minimum or is metastable, Subsection 4.1.2.

3.3.4 System Visualization

In order to visualise the system we use the dump command; this outputs a LAMMPS trajectory file (lammpstrj). This dump file represents a snapshot of our system. These snapshots were collected at 1000 timestep intervals. In this file all atom positions and ids are collected and recorded. This file can then be opened in Visual Molecular Dynamics (VMD) [80] to visualise the various images of the system. The phase behaviour was then classified by eye and global nematic order parameter, S_2 , Subsection 3.3.1.

Chapter 4

Results & Discussion

In this chapter, we split our analysis into two sections. Firstly, we discuss systems of attractive rods and depletant. Following this, we discuss the formation of tactoids in MD and the differences between our MD tactoids and experimental tactoids.

4.1 Rods and the Depletion Interaction

In this section, we will begin by presenting the phase diagram generated by solving the isotropic-nematic coexistence conditions, Section 2.2. We will then present and classify our MD results. Following this, we will compare MD and theory and explain why MD makes for a better comparison with experimental systems. Finally, we will compare MD to prior simulations and the experimental work of Oliveira Silva et al [1].

4.1.1 The Theoretical Isotropic-Nematic Phase Diagrams

Using methods in Sections 3.1.1 and 3.1.3, we obtain the system variables in Table 4.1. Combining these variables with theory outlined in Section 2.2, we then solve the isotropic-nematic coexistence condition for multiple ϕ_r values and obtain the isotropic-nematic phase diagrams, Figure 4.1.

Figure 4.1 (a), is the phase diagram of the reservoir polymer volume fraction ($\phi_{d,R}$) against system rod volume fraction (ϕ_r), while (b) is the phase diagram of system polymer volume fraction (ϕ_d) against the system rod volume fraction. Scanning our theoretical isotropic-nematic phase diagrams we observe 3 distinct regions: isotropic, nematic and isotropic-nematic coexistence. Setting up a system with (ϕ_r, ϕ_d) below the black binodal in Figure 4.1(b) has its thermodynamic minimum as a pure isotropic phase. By contrast

Variable Name	Symbol	Value (units)
Total Length	L_t	70 (nm)
Cylinder Length	L	63 (nm)
Rod Diameter	D	7 (nm)
Radius of Gyration	R_g	3.308 (nm)
Aspect Ratio	R_g/R	0.945 (no units)
Length/Diameter ratio	L/D	9 (no units)
$1 + \frac{L}{D}$	γ	10 (no units)
Spherocylinder Volume	ν_0	$\frac{9947}{12}\pi$ (nm ³)
Excluded Volume	ν_{excl}	3340.4 π (nm ³)

Table 4.1: This Table displays the dimensions and properties of the rod-depletant system.

setting up a (ϕ_r, ϕ_d) system below the orange binodal has its thermodynamic minimum as a pure nematic phase. Any (ϕ_r, ϕ_d) system between the two binodals will have its thermodynamic minimum as an isotropic-nematic coexistence with composition determined by the blue tie lines in Figure 4.1 (b). Note that the tie lines for Figure 4.1 (a) are parallel to the ϕ_r axis and not shown.

We did not need to consider $I_1 + I_2$ or $N_1 + N_2$ phases as our $(L/D, q)$ is beyond the critical endpoint, so no critical points are found for the isotropic and nematic phases, Appendix F.

The Utility and Limitation of our Theory.

Although we have only considered the isotropic-nematic phase diagram, this theory provides a good baseline for us to predict and compare with the outcomes of MD. Comparison between MD and theory early on was used to help determine the number of particles required in our rods, as too few particles during precursor simulations lead to rods being in an isotropic phase at very high ϕ_r values, Subsection 4.1.4. However, the theoretical discussion of phase behaviour only takes us so far as it considers purely thermodynamics. Unlike MD which inherently considers possible metastability/kinetic effects that are often observed in experimental systems, Subsection 4.1.2.

For this work, our theory primarily focuses on the isotropic and nematic phase transition. Consideration of higher order phases such as Smectic C, Smectic A and Crystalline can be done using Free Volume Theory [81, 31, 10] and follows a similar method as in

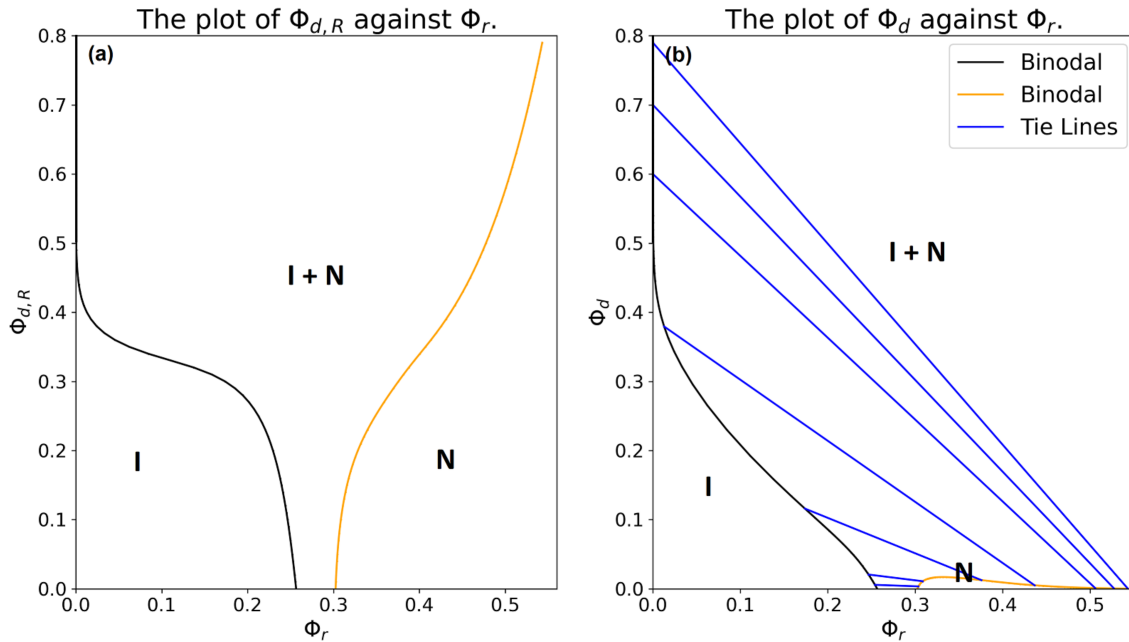


Figure 4.1: This Figure is the isotropic-nematic phase diagrams for a system of rods + depletant with system variables found in Table 4.1. (a) is the reservoir diagram plotting reservoir polymer volume fraction against rod volume fraction. (b) is the system diagram showing system polymer volume fraction against rod volume fraction. The black and orange lines are the binodals and the blue lines are tie lines. Note the tie lines for the reservoir plot are not shown as they are parallel to the rod volume fraction axis.

section 2.2. However, we have chosen to use MD to probe these higher order phases and used the theory as more of a comparative and predictive guide.

Our theory makes a number of approximations and assumptions that we shall briefly cover here.

Firstly, the **penetrable hard sphere** model, Subsection 2.2.1, for polymers is an often used, but severely simplified approximation, as true polymer cannot freely overlap.

Secondly, **Onsager's Theory**, Subsection 2.2.3, makes the assumption of; infinitely thin, rigid, hard rods with no polydispersity. Actual Pf4 virus is relatively rigid but is polydisperse [53] and not hard.

Thirdly, **Free Volume Theory**, Subsection 2.2.2, is a mean field approximation, which considers ensemble average values only, without considering system fluctuations. Furthermore, we make the approximation $\langle V_{free} \rangle = \langle V_{free} \rangle_0$ to obtain (2.20) and (2.26). This approximation assumes that the free volume in a system of hard rods and depletant is the same as the free volume in a system of pure hard rods. This approximation works

well at low ϕ_d but breaks down for high ϕ_d .

The **Odijk/Gaussian approximation** [55, 54], Section 2.2.3 used to solve the isotropic-nematic coexistence condition overestimates the loss of orientational entropy for the pure dispersion of rods meaning the coexistence lines are less accurate at low ϕ_d . When comparing MD with theory, Subsection 4.1.5 both systems assume monodisperse rods and the penetrable hard sphere model.

4.1.2 The MD Phase Behaviour of Attractive Rigid Rods

Using the methods discussed in Chapter 3, we scanned the phase space from $\phi_d : 0 \rightarrow 0.8$ and $\phi_r : 0 \rightarrow 0.5$. Phase classification was done by inspection of the movie output from VMD and comparing to Figure 1.1, Section 3.3. Visual observation allows for a qualitative classification of: orientational, stacking and packing order, Subsection 3.3.1. In combination, with this we have measured the global nematic order parameter (S_2) to aid in classification. All S_2 phase data is detailed in Table 4.2. The S_2 parameter is of limited value in biphasic regions as these likely contains two systems of very different levels of nematic order, we also observe a number of metastable phases for which the order parameter does not capture the observed phase behaviour.

Classification of the Pure Phases

We observed 4 pure phases, Figure 4.2: isotropic (d), nematic (c), smectic C (b) and crystalline/smectic A (a), Figure 4.2.

The **isotropic** phase, Figure 4.2(d), has no nematic order, $S_2 \sim 0$, selectively maximising orientational entropy, with no rod-rod alignment.

The **nematic** phase, Figure 4.2(c), maximises packing entropy at the expense of orientational entropy, $S_2 \sim 0.66$. There was a large ΔS_2 value, Table 4.2, for this system, due to alignment with multiple directors in one of the nematic systems. The average without this anomalous system was $S_2 \sim 0.73$ and is more inline with our theoretical expectations, Subsection 2.2.3.

The **smectic C** phase, Figure 4.2(b), had an $S_2 \sim 0.73$. This is lower than expected but explained by the ‘zig-zag’ structure resulting in alignment to 2 different directors, lowering the S_2 value. Smectic C reached equilibrium when interfacial free energy was mini-

mized. This minimization was achieved when all smectic layers were close touching with maximum rod-rod contact. These systems did not always fill the simulation box indicating that there may be some isotropic + smectic C biphasic character. Some smectic C systems showed signs of metastability in the formation of cavities. One particular smectic C system, (0.45, 0.3) in Figure 4.4, showed PE/TE fluctuations as a result of rods leaving/entering the smectic C interface. These thermal fluctuations further evidence that a number of the smectic C systems are biphasic isotropic + smectic C.

The **crystalline/smectic A** phase, Figure 4.2(a), had an $S_2 \sim 0.92$, this value is high as almost all rods aligned to the same director.

For the isotropic, nematic and crystalline/smectic A phase, equilibrium was established when all of the simulation box was occupied by the pure phase. This is energetically preferred as a filled simulation box has no interface.

The isotropic and nematic showed no consistent nearest neighbor packing (ψ_6) or stacking order(τ), while the smectic C and crystalline/smectic A showed a higher level of packing and stacking order with each rod having 6 nearest neighbors, this is as expected, Subsection 3.3.1.

Classification of the Biphasic Regions

As we have classified the 4 pure phases, we can now discuss the biphasic regions that were observed in MD.

We observed 4 different biphasic systems, Figure 4.3, these include: aligned isotropic (a), isotropic + nematic (b), isotropic + smectic (c) and smectic clusters (d).

The **aligned isotropic** phase, Figure 4.3 (a), lies somewhere in-between isotropic + nematic and isotropic, showing a degree of localised nematic order with no common director, hence $S_2 \sim 0$.

The **isotropic + nematic** phase, Figure 4.3(b), had an $S_2 \sim 0.2$. The order of the nematic component of the system is lowered by the lack of a director in the isotropic phase.

The **isotropic + smectic** phase, Figure 4.3(c), shows regions of smectic character and isotropic character, $S_2 \sim 0.4$.

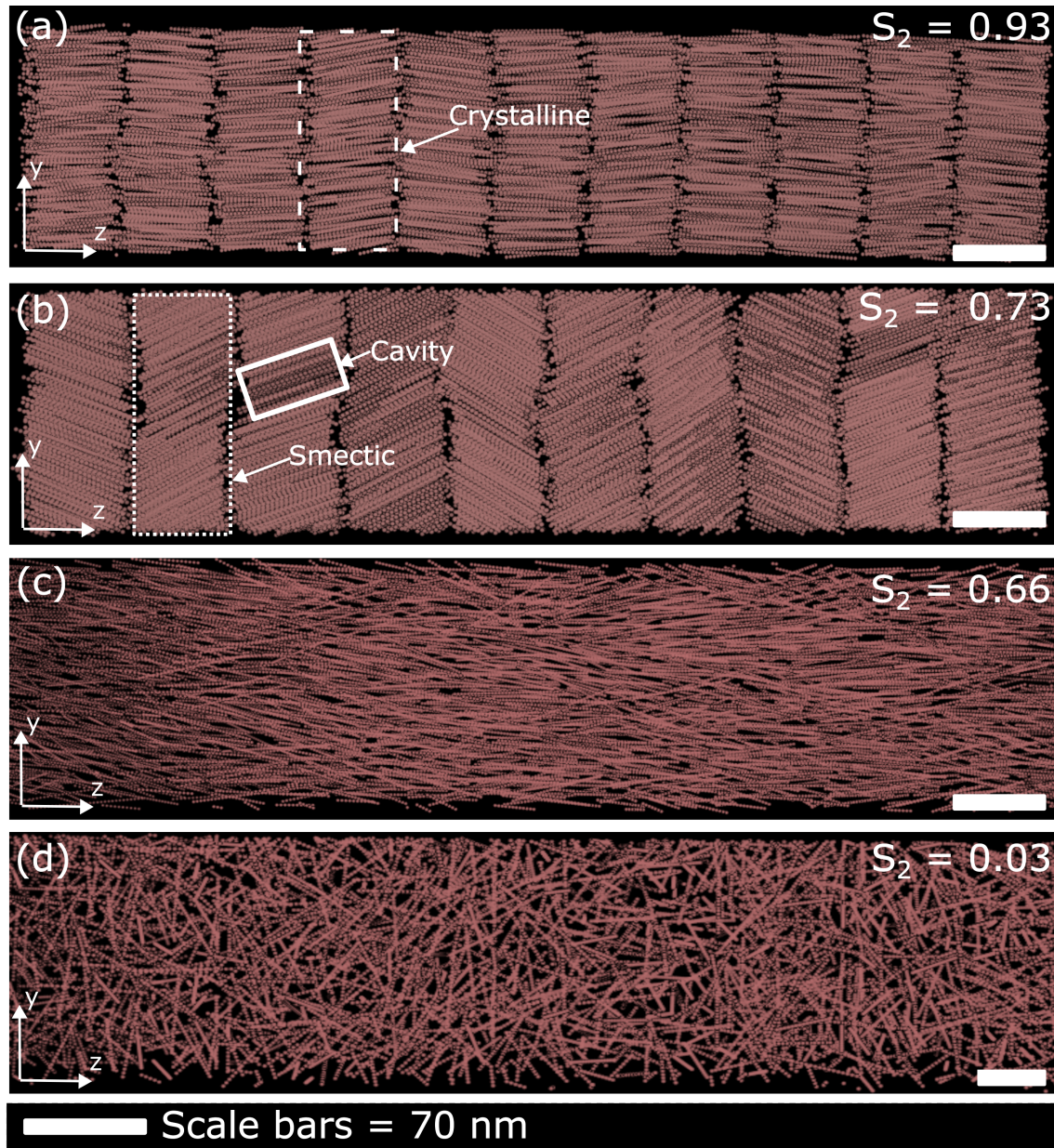


Figure 4.2: This Figure shows the 4 pure phases observed in our MD. (a) is the crystalline/smectic A phase, (b) is the smectic C phase, (c) is the nematic phase and (d) is the isotropic phase. The average S_2 parameters are shown on the diagram. Indicated on the Figure is a crystalline layer, a cavity and a smectic C layer.

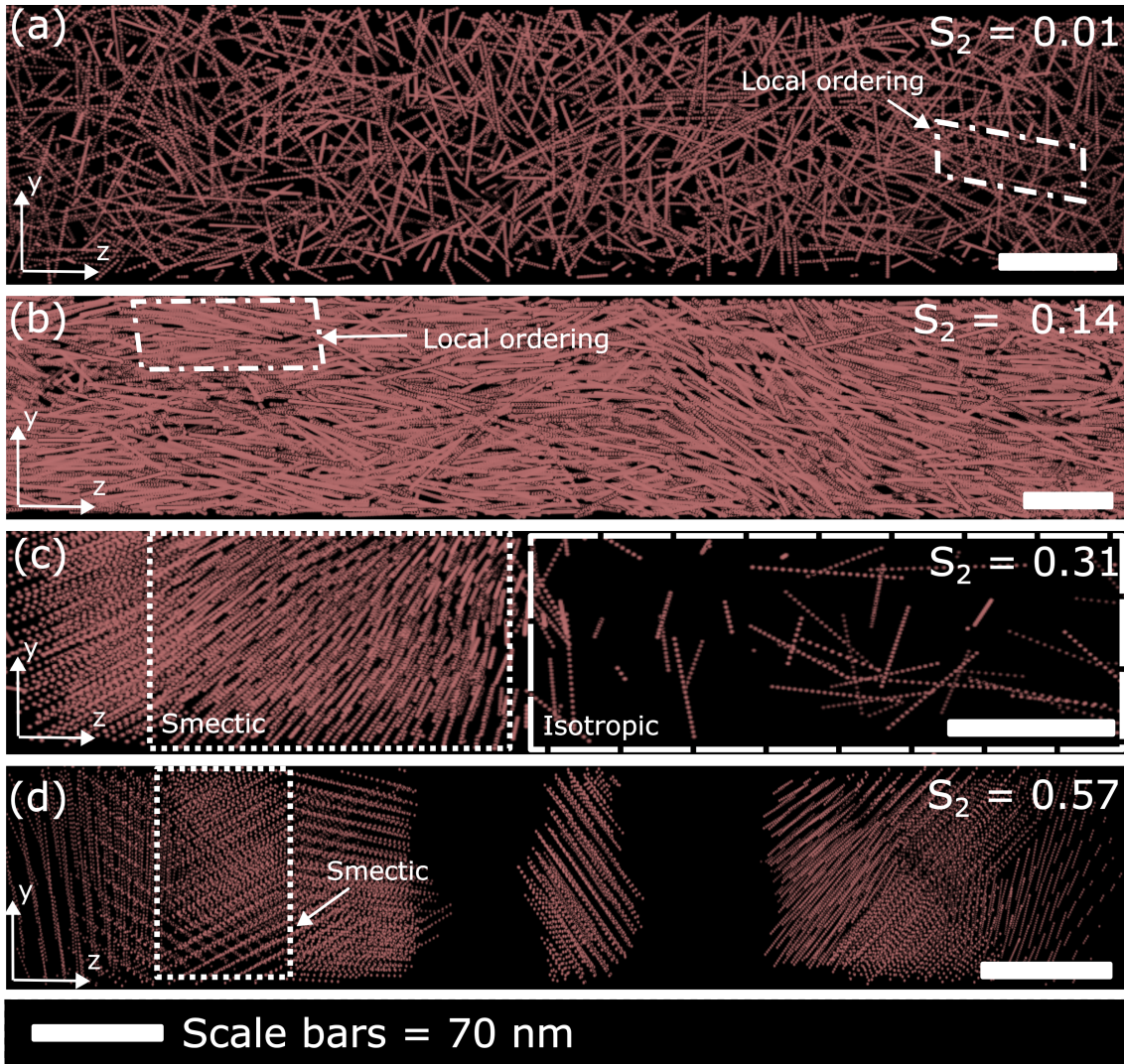


Figure 4.3: This Figure shows the 4 observed biphasic regions. (a) is the aligned isotropic, (b) is the isotropic + nematic coexistence, (c) is the isotropic + smectic coexistence and (d) is the smectic cluster phase. The average S_2 parameters are shown on the diagram. Indicated on the Figure our regions of smectic clusters, isotropic phases and local ordering.

The **smectic cluster** phase, Figure 4.3(d), is a variation of the smectic + isotropic phase, where the isotropic ϕ_r is small meaning that no rods are observed in the isotropic phase for the small number of rods used in the simulation. The $S_2 \sim 0.6$ is larger than the isotropic + smectic due to all rods existing within the smectic clusters. However, both the smectic cluster and isotropic + smectic are lower than smectic C due to reduced nematic alignment of the smectic layers.

The isotropic + smectic and smectic clusters both showed signs of metastability, likely due to either a large cell-rod LJ attraction preventing thermal fluctuations from minimiz-

Phase Type	# of Phase observed	Average S_2	ΔS_2
Isotropic	13	0.029	0.033
Nematic	4	0.658	0.341
Smectic C	21	0.728	0.108
Crystalline/smectic A	2	0.923	0.040
Aligned isotropic	4	0.012	0.003
Isotropic + nematic	2	0.135	0.114
Isotropic + smectic	11	0.311	0.354
Smectic clusters	9	0.569	0.319

Table 4.2: This Table summaries the average S_2 values for the pure and biphasic systems. $\Delta S_2 = \max(S_2) - \min(S_2)$.

ing the interfacial free energy or the presence of rod isotropic rods stopping smectic clusters from combining. The aligned isotropic and isotropic + nematic systems showed no signs of metastability and both reached equilibrium when the simulation box was filled. The smectic cluster and isotropic + smectic systems reached equilibrium when clusters were unable to combine further or had fully combined.

4.1.3 Comparing MD and Theory

As we have presented the theory and classified the phases of MD, we can now compare theory and MD. To do this we overlay our MD points onto the theoretical isotropic-nematic phase diagram from Figure 4.1(b) to obtain Figure 4.4. Scanning Figure 4.4 at constant ϕ_r while varying ϕ_d , we observe 4 different regions within MD. These are summarised in Table 4.3. Any point within these regions in Table 4.3 and Figure 4.4 show similar phase behaviour as ϕ_d increases at constant ϕ_r .

The red point in Figure 4.4, was approaching but did not reach equilibrium in the TE or PE plots as the isotropic had not fully expanded into all of the simulation box. This point has been ignored from the S_2 parameter calculations in Table 4.2.

A initial comparison of theory and MD, shows that as we increase ϕ_r at constant ϕ_d , there is an increase in general order and MD exhibits a far wider range of phases, this is

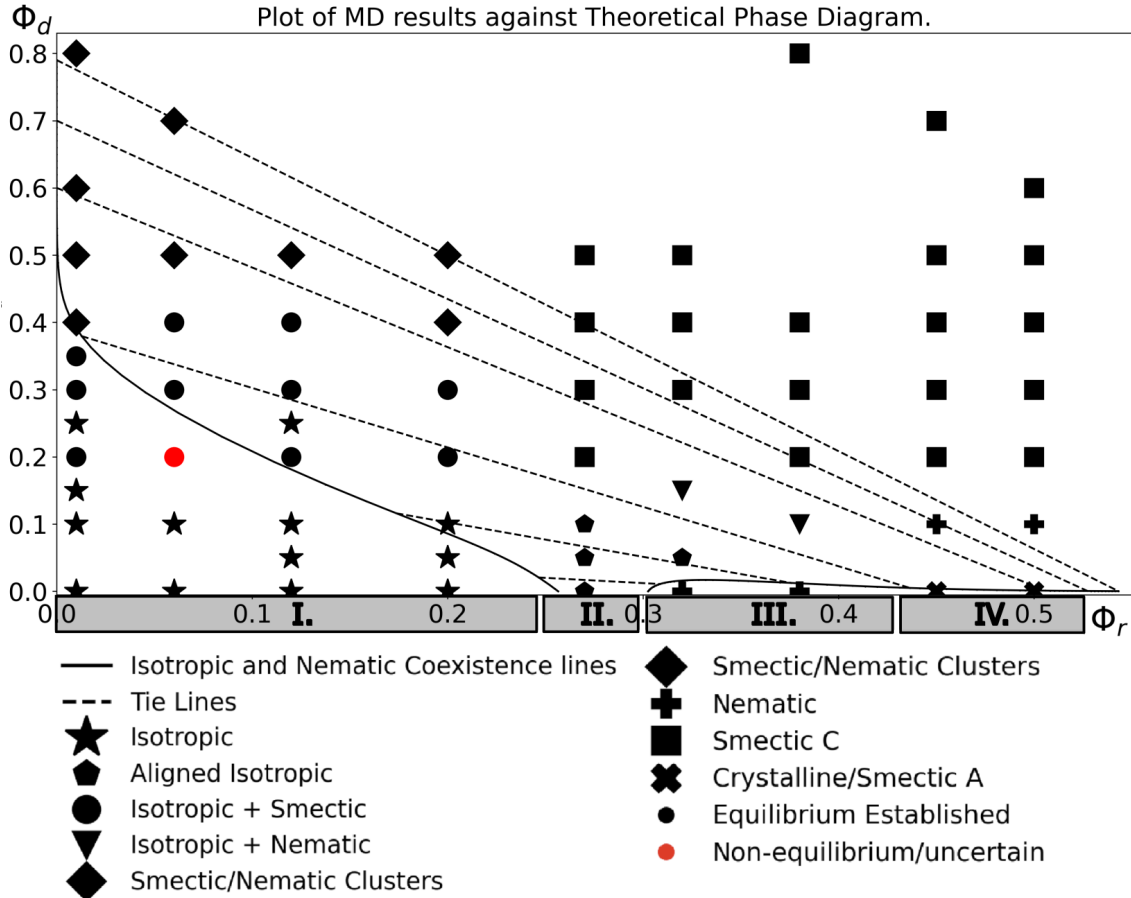


Figure 4.4: This Figure overlays the MD points tested on the theoretical phase diagram in Figure 4.1 (b). I, II, III, IV are regions outlined by the grey boxes, these refer to the 4 regimes in Table 4.4.

to be expected as we did not consider the smectic and crystalline phases in our theory.

The MD isotropic region is smaller than the theoretical prediction. This is likely due to over-fitting the well depth in the 31 particle rod case and over-fitting as a result of only considering the parallel rod configuration in our LJ fitting process, Subsection 3.1.3. 31 particles was used for $\phi_d \leq 0.2$. For $\phi_d \geq 0.25$, 21 particle fitting was used which displayed a later onset of the smectic phase. while, it was necessary to use more particles in rods at lower ϕ_d to insure the rod had overlapping repulsive spheres, this has lead to a discrepancy in the fitting of 21 vs 31 particle rods and as a result a discontinuity at $\phi_d \sim 0.2$ for low ϕ_r .

In MD we observed a very little of the isotropic + nematic coexistence, this is most likely due to our theory not considering higher order phases and theory not accounting for the existence of metastability. Previous simulations have confirmed the existence of

Region Label	Approximate ϕ_r Range	Phase Transitions as ϕ_d	Changes in S_2
I	0 → 0.25	Isotropic → Isotropic + Smectic → Smectic clusters	0.03 → 0.35 → 0.57
II	0.25 → 0.3	Aligned Isotropic → Smectic C	0.01 → 0.73
III	0.3 → 0.42	Nematic → Isotropic + Nematic → Smectic C	0.66 → 0.2 → 0.73
IV	0.42 → 0.5	Crystalline/Smectic A → Nematic → Smectic C	0.92 → 0.66 → 0.73

Table 4.3: This Table describes the main MD regions of ϕ_r illustrated in Figure 4.4 by grey transparent bars.

a thermodynamically stable smectic phase [31, 10, 82] validating our observations of the smectic C.

The aligned isotropic found in regions where the theory predicts isotropic-nematic coexistence is likely due to the imperfect nature of the LJ fitting method with insufficient LJ attraction to create a distinguished nematic region. This could also be caused by the inaccuracy of the Gaussian orientational function at low ϕ_d , Subsection ??.

MD is more appropriate for comparison with experimental systems as our theory only covers the isotropic-nematic coexistence and our theory does not consider the effects of metastability/kinetics. Subsequent comparisons with prior simulations and experimental will be done with MD, as MD more accurately encapsulates the phase behaviour of rod-like colloid + depletant systems than our theoretical phase diagram.

4.1.4 Comparing MD Results to previous Simulation work

There are two main simulation points of comparison that I have considered. Firstly, prior simulations of suspensions of purely repulsive rods [83] and secondly, simulations of the depletion interaction with explicit polymer [2].

Comparing my MD to prior repulsive rod simulations, Table 4.4, tests the effectiveness of the overlapping sphere rod model. Purely repulsive simulations were performed at $\phi_d = 0$, which used a WCA potential between rods. A comparison of our MD with the MC simulations of Bolhuis et al [10] shows very similar phase behaviour. This agreement of MD and MC validates our use of spherical bead rods and the WCA potential for rod-rod repulsion.

Calero et al [2] used the overlapping sphere rod model with explicit spherical depletant. We also tried this but found it to be computationally expensive and challenging

Type of Simulation Method	L/D ratio	Isotropic ϕ_r range	Nematic ϕ_r range	Smectic A/Crystalline ϕ_r range
Molecular Dynamics	9	0 - 0.3	0.3 - 0.42	0.42 - 0.5
Monte Carlo	8.62	0 - 0.3	0.3 - 0.45	0.45 - 0.6

Table 4.4: This Table provides a comparison of my MD results to the MC results of Bolhius et al [10].

Polymer Type	L/D ratio	aspect ratio	# of rods in the system.	# of particles per rod.
implicit	9	0.95	1000 or 2000	21 or 31
explicit	20	1.2	125	194

Table 4.5: This Table compares the properties of our system with those of Calero et al [2].

to implement for high rod volume fraction systems. The LJ fitting, Subsection 3.1.3, allowed us to perform simulations at a variety of concentrations at low computational expense. Despite the lower accuracy of the LJ fitting approach, there does seem to be in qualitative agreement between our MD and the results of Calero et al. Table 4.5 displays the different system variables between us and Calero et al, which prevents a quantitative comparison from being made.

Figure 4.5(b) shows instances of a number of different smectic A, smectic C and isotropic + smectic phase behaviour. Figure 4.5(b1) clusters are similar to the layers found in Figure 4.2 (b). (b2) and (b3) clusters are observed in our Figure 4.2(a) crystalline/smectic A phase. Finally, (b4) is observed in Figure 4.3(c-d). These simulation similarities indicate that metastable phase behaviour is common when simulating systems that involve the depletion interaction with rods.

The agreement of our MD with the work of Calero et al [2] and Bolhius et al [83] validates our model. We can move on to compare MD with the experimental phase behaviour of de Oliveira Silva et al [1].

4.1.5 Comparing MD and Experimental Phase Behaviour

The work of de Oliveira Silva et al [1] involved experimentation on systems of Pf4 virus in the presence of sodium alginate, there are the systems on which our MD is based. Figure 4.6 and Figure 1.2 show the experimental phases observed by de Oliveira Silva et al [1]. The substantial difference in L/D and q between our MD and the experimental

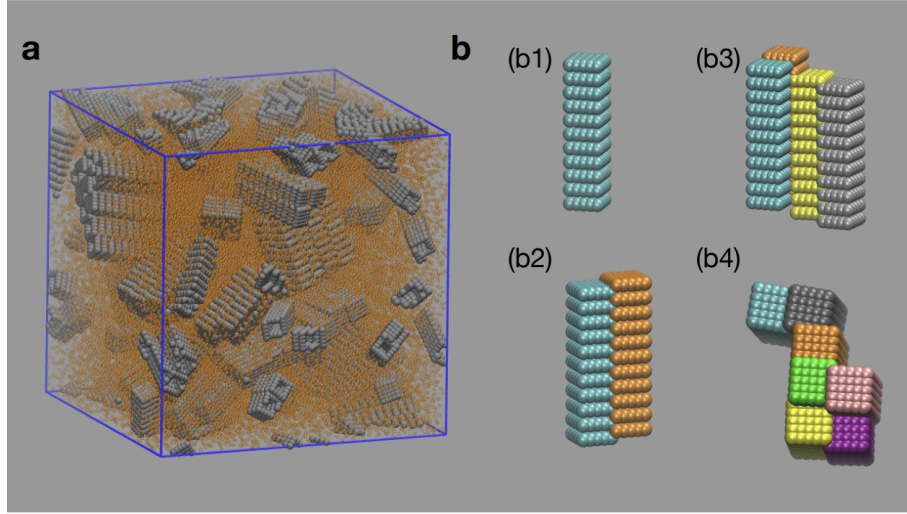


Figure 4.5: This Figure is taken from [2] with the figure description. (a) Snapshot of simulated system. The spherical beads forming the rods are represented in gray. Depletant particles are represented by orange beads. (b) Frequent assemblies observed in simulations.

system, Section 3.1, makes a quantitative comparison impractical but we can still make some qualitative comparisons.

Figure 4.6 (a) illustrates that as ϕ_d and ϕ_r increases, the level of nematic ordering increases. Tactoids (c) and networks (d) are formed in the theoretical isotropic-nematic coexistence region. The experimental isotropic phase is observed in a similar region to the MD isotropic region, Figure 4.4.

Tactoids and networks are both metastable, tactoids are droplets of the nematic phase and likely do not form a single nematic region due to high solvent viscosity or small differences in phase density resulting in slow tactoid sedimentation [84]. Networks show connections between tactoids, Figure 4.7.

Similar to experimentation our MD shows lots of metastable phase behaviour, section 4.1.2, in the form of isotropic + smectic and smectic clusters. These are analogous to the tactoids and networks in the Pf4 virus experimental systems. The connecting of multiple tactoids in the networks shows a degree of stacking order, Figure 4.7 (a), that is similar to the stacking in smectic C.

The large differences in: aspect ratio, L/D , dispersity, solvent viscosity and mass make any further comparison more difficult. To obtain further insight on tactoid formation, we should perform MD with polydisperse rods and modelling with polymer that has

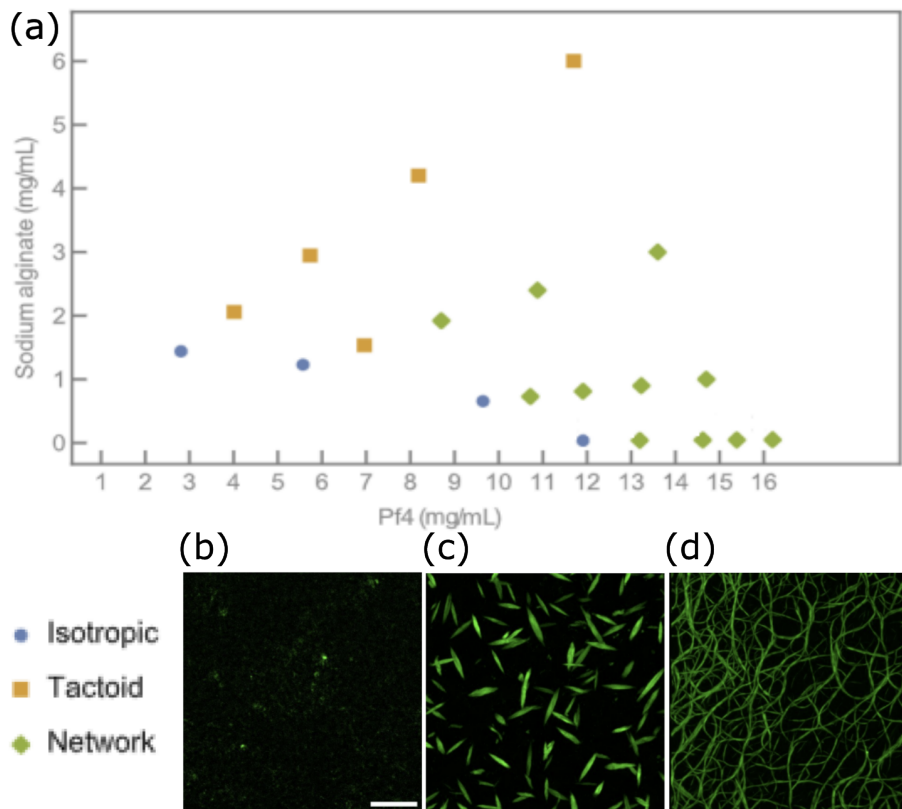


Figure 4.6: This Figure is the experimental phase diagram of [1]. (a) is the experimental phase diagram, (b) is an example isotropic phase, (c) is an example tactoid phase and (d) is an example network phase. The scale bar is $20\mu\text{m}$.

a larger radius of gyration.

Succeses and Limitations of MD.

MD focuses on the stability and kinetics of the system rather than exclusively thermodynamics, making comparison between MD and experimentation more insightful than exclusive comparison between theory and experimentation. While MD of attractive rods has shown to be effective at mirroring experimentation, it is not without limitations. A number of which are listed below.

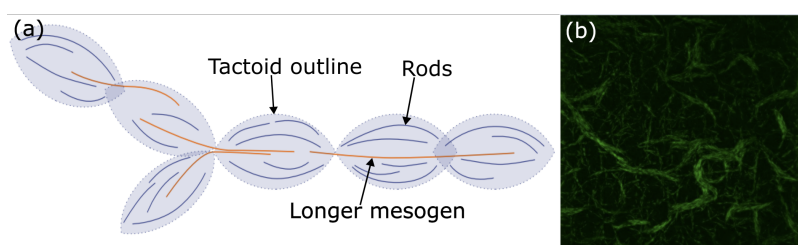


Figure 4.7: This Figure [1] shows the observed network structures. (a) is a cartoon image of the tactoid aligning in networks and (b) is a network image. The scale bar is $20\mu\text{m}$

Firstly, the LJ potential fitting of the depletion interaction, Subsection 3.1.3, only considers the parallel case of rods, this leads to over-estimation of the required well depth. The LJ potential fitting does not work for large radius of gyration values, at it fails to effectively fit the steep repulsion and short ranged attraction simultaneously for these cases.

Secondly, the overlapping sphere approach is computationally expensive at **large** L/D and **low** ϕ_d as both require a very large number of spheres per rod to accurately model rod phase behaviour. This meant we had to use 21 and 31 particle rods which lead to its own phase discrepancies, Section 3.1.1 and 4.1.5.

Finally, the initial crystalline alignment of rods struggles to reach equilibrium at low ϕ_r due to the time taken for the isotropic phase to expand throughout the cell. Also our systems only use 1000 or 2000 rods, this means that systems which contain a high ϕ_r smectic phase in coexistence with a low ϕ_r isotropic phase, appear to have empty space, when a large enough simulation would contain a small quantity of rods within the isotropic phase.

4.1.6 Summary for Rod + Depletant Systems

In this section, we have presented our theory and classified/described our MD results. We have then compared the theory to MD and validated our MD results against prior simulation work and the experimental system on which our MD is based.

For better comparison with experimentation, we need to perform simulations using larger L/D ratios, rods that are polydisperse and depletion interactions with longer ranges.

For more objective classification of the phases, we should have calculated the smectic order parameter (τ) and hexatic order parameter (ψ_6) to identify the smectic and crystalline phases respectively [33, 32, 85]. Given more time I would have calculated these order parameters quantitatively and would of further expanded by theory to consider higher order phases.

4.2 Generating Tactoids in MD

In the previous section, we validated our use of MD to simulate systems of rod-like colloids + depletant. We will now extend this using methods in Chapter 3 to generate tactoids. Then we will comparing our tactoids to experimental tactoids [1].

4.2.1 Imaging of Tactoids in Rod-like Colloid Isotropic Phases

Figure 4.8 (ai-iii) illustrates a number of different experimental tactoids, while (b-d) are images of MD tactoids coexisting in the rod isotropic phase. These systems obtained dynamic equilibrium quickly, following the formation of multiple layers of rods around the cell. Figure 4.8 (c) and (d), show close ups of the tactoid. The rods on the inside of the tactoid vibrationally oscillate around their relatively fixed positions, while the outer rods of the tactoid are less ordered and exchange with rods in the isotropic phase. Dynamic equilibrium in this case is defined by, tactoid rod loss rate = tactoid rod gain rate, meaning the tactoid is no longer increasing in size.

We can see that multiple layers form around the cell, with areas of the rods adhered to the cell showing higher levels of localised order, see Figure 4.9 (a-d). Some areas of local order appear to align along different directors to the majority of the rods. This metastability is because thermal fluctuations are insufficient to overcome the rod-cell LJ potential which holds rods in place.

Figure 4.9 (a) and (c) are cross-sectional images of the tactoid. These demonstrate the similarity between the inner layers and the smectic C/smectic clusters found in section 4.1.2. The average thickness of the tactoid seems to be around 4 rods, the innermost and outermost rods have 4 nearest neighbors while the rods in the central layers have 6 nearest neighbors.

The global S_2 value for tactoid systems was 0; this does not reflect the degree of orientational order within the tactoid for 2 reasons. Firstly, the majority of rods are found in the isotropic phase, suppressing the S_2 . Secondly, the clusters on opposite ends of the tactoid align to opposite directors and cancel one another out.

(a) and (c) in Figure 4.9 indicate that there is strong rod-cell anchoring, as a consequence of the large rod-cell LJ potential. The type of anchoring observed is known as degenerate planar anchoring [1, 86] see Subsection 4.2.3. These images also show a degree of rotational order/chirality around the cell. This was not found in all of my tactoids, but the degree of rotation appeared to be higher for larger LJ attraction parameters. As we have not quantitatively measured, we cannot be certain that this effect is cancelling out,

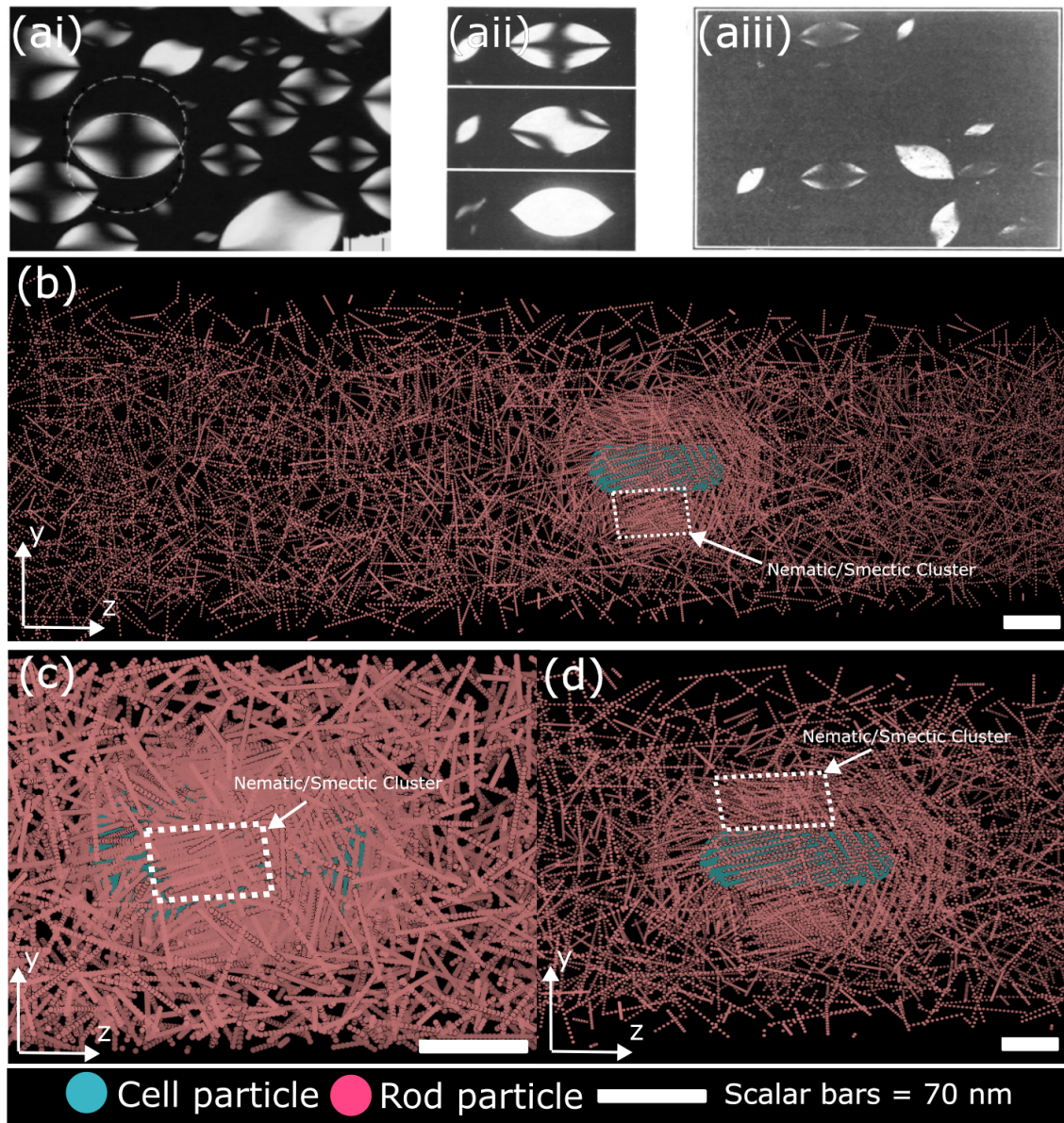


Figure 4.8: This Figure shows multiple images of the long cell tactoids and experimental tactoids. (a) SEM Images from [3](ai) vanadium pentoxide [4], (a(ii)) aluminium oxyhydroxide [5], (a(iii)) TMV [6] and (a(iv)) schematic of nematic tactoids with homogeneous, intermediate and bipolar director field configurations formed in carbon nanotube dispersions [7]. (b) Image of long cell tactoid and isotropic coexistence, (c) and (d) close up images of tactoids. Example regions of nematic/smectic clustering are labelled in (b-d).

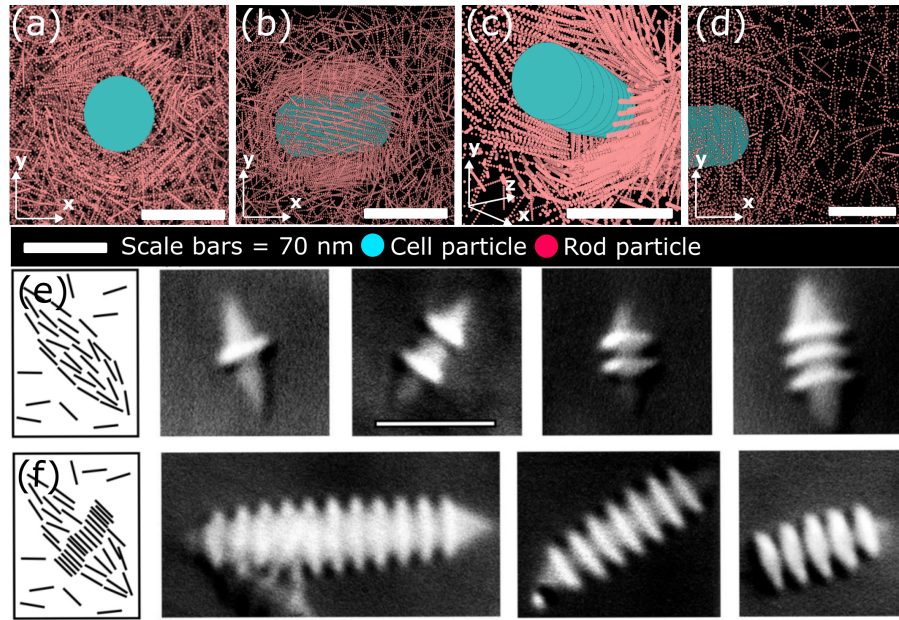


Figure 4.9: This Figure shows close up images of tactoid for comparison with experimental tactoids. (a-d) Images of MD tactoids from different perspectives, (e) theoretical and experimental SEM images of nematic tactoids [8] and (f) theoretical and experimental SEM images of smectic tactoids [8].

see Subsection 4.2.3.

Figure 4.9 (b) and (d) shows the spherical cap of the tactoid, this has a thinner layer of rods compared to the barrel of the tactoid. The cap has a more spherical and less aligned shape when compared to the experimental tactoids in Figure 4.9 (e-f) and 1.2. This is likely due to differences in rod-cell anchoring strength, see section 4.2.3.

Figure 4.9 (e) and (f) [8], illustrate the structure of nematic and smectic tactoids. Figure 4.9 (a-c), show rod alignment along the barrel more closely resembling (f) but end alignment that is more spherically capped than (e) or (f), see Subsection 4.2.3.

4.2.2 Generating Tactoids under Different Conditions

To further investigate tactoid formation we varied a number of different parameters of our simulation including: rod-cell LJ potential strength, ϕ_d (rod-rod LJ strength) and finally cell length. Figure 4.10 (a-c) illustrates the effect of varying ϕ_d /**rod-rod LJ strength**. In Figure 4.11. three values of ϕ_d : 0 (a), 0.25 (ab) and 0.5 (c) are shown but multiple values were tested. All 3 systems obtained equilibrium, Subsection 3.3.3, however it is likely that (c) is metastable.

Figure 4.10 (a) and (b) both show the formation of a stable tactoid that has reached

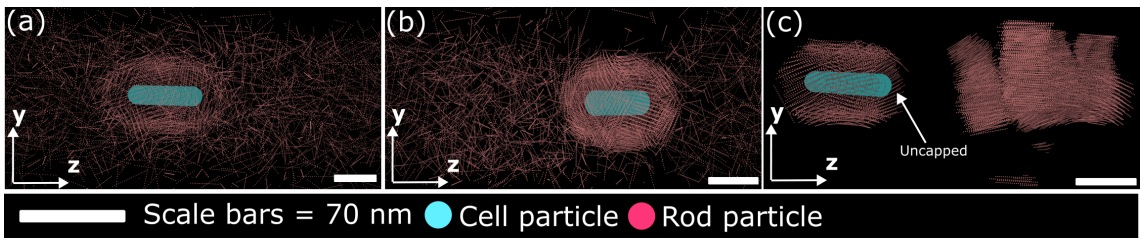


Figure 4.10: This Figure shows the tactoid formation under 3 different depletant concentrations. (a) $\phi_d = 0$, (b) $\phi_d = 0.25$ and (c) $\phi_d = 0.5$

dynamic equilibrium with the isotropic phase. In the case of (b), the tactoid is noticeably thicker. For $0 < \phi_d < 0.3$, thicker tactoids were observed than the $\phi_d = 0$. For $\phi_d \geq 0.3$ formation of incomplete tactoids or weaker layering was observed. Tactoid size appears to be enhanced by the depletion interaction between rods, up until smectic/nematic phase behaviour is observed independent from the cell. However, the main driving force of tactoid formation was the direct rod-cell LJ attraction.

Figure 4.10(c) appears to form a partial tactoid and smectic C phase. This is metastable as the adherence of the rods to the cell is energetically preferable. Thermal fluctuations are insufficient to allow the rods to leave the smectic C and adhere to the cell.

The rod-cell LJ attraction is maximised along the barrel of the cell, this justifies why the caps show thinner layering than the barrel of the tactoid, Figure 4.9(d), and why the rods that do adhere in case Figure 4.10(c) are adhering to the barrel of the cell, not the ends of the cell. During the formation of all tactoids, the rods adhere to the barrel first.

A range of **rod-cell LJ attractions** were tested. Figure 4.11 (a) and (b) show rod-cell LJ $\epsilon = 0.3 k_b T$ and $2.0 k_b T$ respectively. Below a certain value no tactoid formation was observed, following this there was an increase in layer thickness with diminishing returns at higher ϵ values, Figure 4.11 (c) and (d). At higher rod-cell ϵ values, there was more LJ clustering and less alignment along the barrel of the cell. The degree of twisting also showed an increase with higher ϵ . This is likely due to the increase in anchoring as LJ attraction increases, see Subsection 4.2.3.

Finally, **Two cell types were tested**, short cells and long cells, Subsection 3.1.3. The properties of these were largely the same, with the main differences being steeper shape of the spherical cap, lower levels of layering and greater preference for rods aligning to

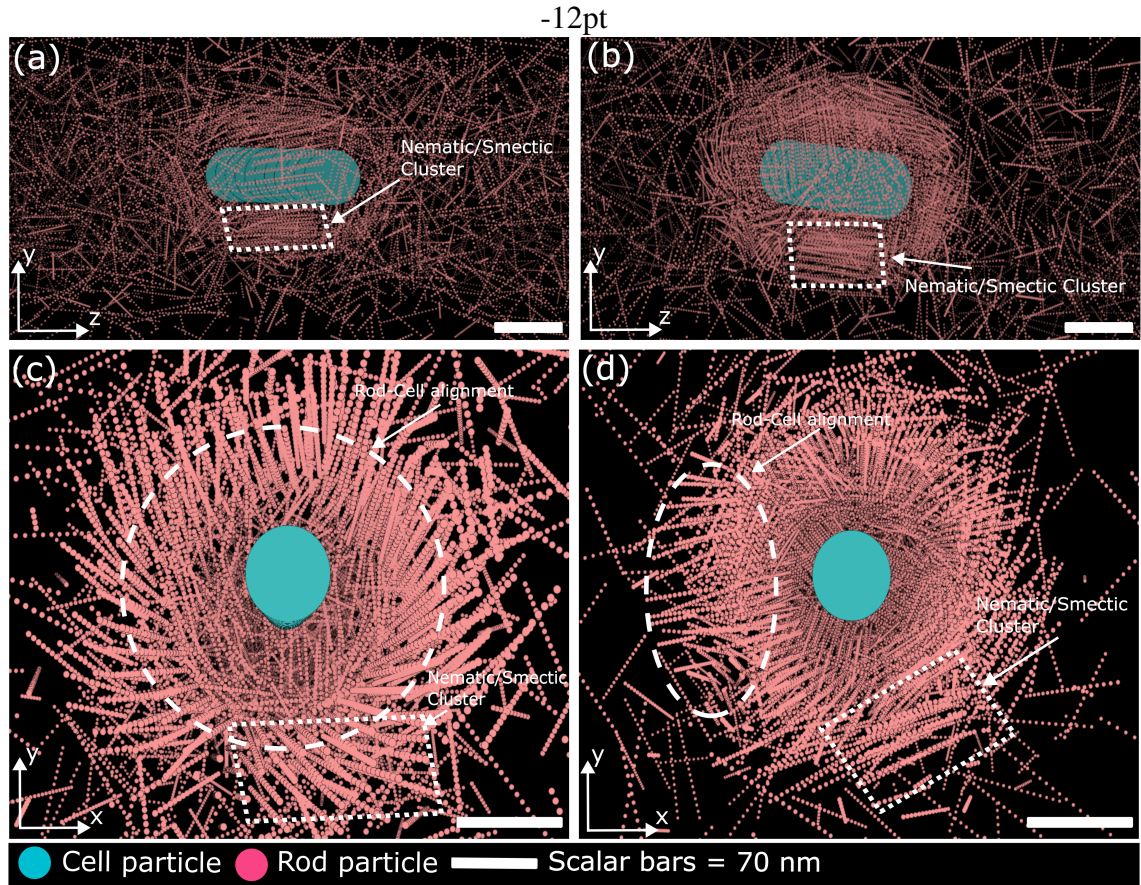


Figure 4.11: This Figures shows images from different cell-rod LJ ϵ values. (a) and (c) $\epsilon = 0.3$. (b) and (d), $\epsilon = 2.0$. (a) and (b) are side on tactoid images. (c) and (d) are cross-sectional views. Some regions of rod-cell alignment and smectic/nematic clusters are indicated on the diagram.

the barrel in the short tactoid. As we have discussed the imaging and properties of our tactoids, we will now discuss the difference between tactoids generated in MD and those found in experimental systems [1].

4.2.3 Comparing MD and Experimental Tactoids

In order to compare tactoid shape/dynamics we must briefly introduce some theory on the formation of tactoids and what determines their shape.

Tactoid formation occurs via either spinodal decomposition or nucleation and growth [1]. Tactoid formation in MD occurred on a rod by rod single binding basis. Our tactoids form in the thermodynamically stable isotropic phase due to strong rod-cell LJ interactions. This suggests that the tactoids are forming as a consequence of nucleation and growth as seen experimentally by de Oliveira Silva et al [1]. Spinodal decomposition to form tactoids in experimental systems typically occurs for shorter rods and higher cell

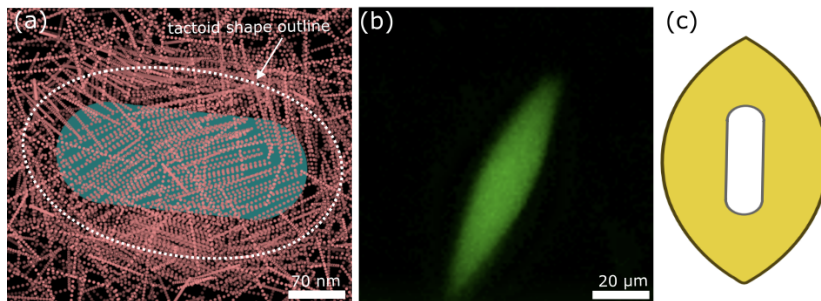


Figure 4.12: This Figure shows the MD, experimental and theoretical tactoid shapes expected. (a) is a birds-eye-view image taken from my tactoid simulations, (b) is an image of an experimental tactoid from [1] at the following: Pf4 (mg/mL) = 1 and Sodium alginate (mg/mL) = 2.5 and (c) is an image of a typical theoretical tactoid with cell encapsulation, taken from Figure 5.4 of [1].

concentrations [1].

Tactoids shapes are primarily determined by a balance of surface and elastic effects. Surface effects include surface tension and anchoring [1]. Surface tension is minimised by reducing interface size between two different phases and anchoring involves maximization of surface force interactions. The anchoring we are focusing on is the rod-cell anchoring over the rod-isotropic phase anchoring. Elastic free energy focuses on the energy cost associated with incomplete alignment increasing free energy, described by the Oseen-Frank Energy [1]. For further details on anchoring, see [87] and for elastic energy, see [88].

In MD, the strong LJ attraction between rod and cell, means we are in the strong anchoring condition (Dirichlet boundary conditions), favouring a more curved/spherical surface at the expense of elastic free energy. In this case the main elastic free energy is known as splay and bend energy [88]. The tangential (degenerate planar) anchoring orientation found in MD, Subsection 4.2.1, indicates the contrived nature of MD as the strong anchoring regime differs from experimental LCs [1]. As we increased rod-cell LJ attraction, Figure 4.11 (c) and (d), the level of rod-rod alignment around the cell appears to decrease and more localised clustering is observed, this suggests that anchoring has increased and elastic effects are becoming less significant.

Experimental systems, Figure 4.12(b), typically exhibit weaker rod-cell anchoring meaning greater rod alignment is observed to minimise elastic free energy. This results in a more elongated spindle-like tactoid shape.

One final point worth discussing is the possible presence of spontaneous chirality not observed in the experimental tactoids [1], Subsection 4.2.1, this was also observed in some smectic clusters at high rod-rod LJ attraction as well. Chiral symmetry breaking has been observed experimentally in achiral tactoidal lyotropic LCs [89] and in MD as a consequence of strong anchoring (Dirichlet boundary conditions) in systems [86, 90]. Figure 4.9 (a) and (c) show signs of rotational order that could be a consequence of chiral symmetry breaking. The most likely explanation of this, given greater prevalence at higher LJ attractions is strong anchoring breaking symmetry as a consequence of the saddle splay elasticity [86, 90]. This needs to be investigated further to determine the cause or if it is present/if the chirality cancels out.

4.2.4 Summary of our Tactoids

The ability to generate tactoids in MD could further enhance our understanding of the formation of tactoids in experimental systems and CF patients.

Our MD tactoids share a number of similar characteristics with the experimental tactoids [1]. However, further investigation is required to attempt to generate tactoids that are more similar in shape to those of experimental systems.

Chapter 5

Conclusion and Outlook

5.1 Chapter Summary

In chapter 1, we introduced the colloidal domain and the depletion interaction. We then discussed our biological motivation to further understand the formation of tactoids LCs and the reasons for using molecular dynamics. In chapter 2, we outline the features of molecular dynamics and langevin dynamics. Following this we discuss the theory used to solve the isotropic-nematic coexistence condition. Chapter 3, outlined our model for our rods, cells and the depletion interaction. We also detailed the implementation of LAMMPS and how to monitor our MD. Finally, in Chapter 4 we first present and compares our theoretical phase diagram and MD results. We then compare our Rod + Depletant MD results to the experimental systems. Following this we discuss MD tactoids and compare them to experimental tactoids.

5.2 Outline of Results

The boundaries of the theoretical phase diagram shows good agreement with our MD. Although in MD we observed higher order and metastable phases. Comparing our MD to repulsive rods [10] and explicit solvent simulations [2] validate our MD model. Comparison between experimentation and MD shows good qualitative agreement.

Using MD, we have managed to generate tactoids in coexistence with the isotropic phase. These tactoids show a different shape to the experimental tactoids [1] likely due to differences in anchoring strength.

Hopefully, the generation of tactoids in MD will further enhance our understanding of how and why tactoids form around *P.Aeruginosa* in Pf4 virus and sodium alginate.

5.3 Future Work

To further the work done in the rod + depletant systems, MD should be performed with larger q and L/D values, so a quantitative comparison can be directly made to the experimental Pf4 virus phase behaviour [1]. Quantitative characterisation of the MD phase behaviour using τ and ψ_6 should also be performed to better characterise the observed phases.

Finally, attempting to form tactoids in MD under more rod and cell conditions/dimensions will help to enhance our understanding of experimental tactoid formation.

Bibliography

- [1] M. de Oliveira Silva. Tactoid formation in suspensions of pf4 virus particles and the role of impurities, 2022.
- [2] I. Pagonabarraga C. Calero. *Entropy*.
- [3] M. J. Maclachlan P. X. Wang. *PTRSA*, 2018.
- [4] A. V. Kaznacheev et al. *J. Exp. Theor. Phys.*, pages 57–63, 2002.
- [5] C. Trk H. Zocher. pages 140–144, 1960.
- [6] F. C. Bawden et al. *Z. Anorg. Allg. Chem.*, pages 91–110, 1936.
- [7] V. Jamali et al. *Phys. Rev. E*, 2015.
- [8] S. Fraden Z. Dogic. *Phil. Trans. R. Soc. A*, pages 997–1015, 2001.
- [9] R. Tuinier H. N. W. Lekkerkerker. Springer, 2011.
- [10] D. Frenkel P. Bolhuis. *J. Chem. Phys*, 106(2):666–687, 1997.
- [11] D. H. Everett. Manual of symbols and terminology for physicochemical quantities and units, appendix ii: Definitions, terminology and symbols in colloid and surface chemistry. *Pure Appl. Chem*, 31(4):577–638, 1972.
- [12] M. Faraday. 1857.
- [13] W. B. Russel et al. Cambridge Monographs on Mechanics. CUP, 1989.
- [14] F. Oosawa S. Asakura. *J. Chem. Phys*, 22(7):1255–1256, 2004.
- [15] L. Onsager. *Ann. N. Y. Acad. Sci.*, 51:627–659, 1949.
- [16] J. Prost P. G. de Gennes. OSP. Clarendon Press, Oxford, 2nd ed edition, 1993.
- [17] F. Bawden et al. *Nature*, pages 1051–1052.
- [18] Yves Bouligand. *Comptes Rendus Chimie*, 11(3):281–296, 2008.
- [19] Park et al K. *Nano. Letters*.
- [20] D. Baranov et al. *Nano. Letters*, 2010.

- [21] HU Medical Review Board. <https://cystic-fibrosis.com/statistics>. 2023.
- [22] S. D. Freedman B. P. O'Sullivan. *The Lancet*, 373(9678):1891–1904, 2009.
- [23] J. Wingender H. C. Flemming. *Nat. Rev. Microbiol.*, 8:623–633, 2010.
- [24] *Clin. Microbiol. Rev.*, pages 191–206, 1991.
- [25] A. K. Tarafder et al. *Proc. Natl. Acad. Sci. U. S A.*, 117:4724–4731, 2020.
- [26] K. E. McElroy et al. *PNAS*, 111(14), 2014.
- [27] P. R. Secor et al. *Cell Host Microbe*, 18:549–559, 2015.
- [28] J. Meller. Molecular dynamics. 2001.
- [29] B. Smit D. Frenkel. volume 50. 2nd edition, 1996.
- [30] T. Biben et al. *J. Condens. Matter Phys.*, 8(50):10799, 1996.
- [31] S. C. McGrother et al. *J. Chem. Phys.*, 104(17):6755–6771, 1996.
- [32] B. De Braaf. *J. Chem. Phys.*, 147(24), 2017.
- [33] M. Oshima Menegon. PhD thesis, Applied Physics and Science Education, 2019.
- [34] I. Newton et al. Daniel Adee, N.Y., 1846.
- [35] D.G.A.L. Aarts. Lecture notes: Soft condensed matter. 2020.
- [36] J. de Paula P. Atkins. W.H. Freeman and Company, N.Y., 8th edition, 2006.
- [37] A. Gythiel D.S. Lemons. *C. R. Acad. Sci.*, 1997.
- [38] G. Stokes. *Trans. Cambridge Philos.*, 9:8, 1851.
- [39] D. J. Tildesley M. P. Allen. *Computer Simulation of Liquids: Second Edition*. OUP, 2017.
- [40] T. L. Hill. Dover Publications, 1986.
- [41] Sandia Corporation. <https://docs.lammps.org/intro.html>. 2023.
- [42] Sandia Corporation. <https://www.lammps.org>. 2023.
- [43] A. P. Thompson et al. *Comp. Phys. Comm.*, 271:108–171, 2022.
- [44] A. Vrij. *Pure. Appl. Chem.*, 48:471–483, 1976.
- [45] A. Vrij H. de Hek. *J. Colloid Interface Sci.*, 84:409–422, 1981.
- [46] M. S. Wertheim. *J. Stat. Phys.*, 1986.
- [47] A. P. Gast et al. *J. Colloid Interface Sci.*, 109(1):161–171, 1986.
- [48] H. N. W. Lekkerkerker et al. *EPL*, 20(6):559, 1992.

- [49] R. Tuinier G. J. Fleer. *Adv. Colloid Interface Sci.*, 143(1-2).
- [50] B. Widom. *J. Chem. Phys.*, pages 2808–2812, 2004.
- [51] M.A. Cotter. *J. Chem. Phys.*, 66(3):1098–1106, 2008.
- [52] H. Kamerlingh Onnes. *KNAW Proceedings*, pages 125–147, 1902.
- [53] H. N. W. Lekkerkerker G. J. Vroege. *Rep. Prog. Phys.*, 55:1241, 1992.
- [54] H. N. W. Lekkerkerker T. Odijk. *J. Phys. Chem.*, 89(10):2090–2096, 1985.
- [55] T. Odijk. *J. Macromol. Sci.*, 19(9):2313–2329, 1986.
- [56] R. van Roij. *Eur. J. Phys.*, 26:57, 2005.
- [57] T. van Westen et al. *Chem. Phys.*, 140(3), 2014.
- [58] G. Lasher. *Chem. Phys.*, 53(11):4141–4146, 2003.
- [59] J. Herzfeld et al. *J. Macromol. Sci.*, 17:1718–1723, 1984.
- [60] P. van der Schoot T. Odijk. *J. Chem. Phys.*, 1992.
- [61] A. Mori et al. *Mater. Phys. Mech.*, 6:49–57, 2003.
- [62] Y. Tang. *J. Chem. Phys.*, 136(3), 2012.
- [63] M. Whiteley S.P.Diggle. *Proc Biol Sci.*, 166, 2020.
- [64] J. E. Lennard-Jones. *Math. Proc. Cambridge Philos.*, 27(3):469–480, 1931.
- [65] J. E. Lennard-Jones. *Proc. Phys. Soc.*, 43(5):461, sep 1931.
- [66] P. Virtanen et al. *Nat. Methods.*, 17:261–272, 2020.
- [67] G. Van Rossum et al and Fred L Drake Jr. Centrum voor Wiskunde en Informatica Amsterdam, 1995.
- [68] A. Banerjee et al. *Carbohydr. Polym.*, 277:118855, 2022.
- [69] J. D. Weeks et al. *J. Chem. Phys.*, 54(12):5237–5247, 09 2003.
- [70] S. K. Mishra et al. *J. Inequal. Appl.*, 2021.
- [71] S.A. Gorbunov et al. *Com. Phys. Comm.*, 279:108–454, 2022.
- [72] L. Boltzmann. pages 17–560, 1868.
- [73] L. D. Landau. Pergamon Press, 3rd edition, 1980.
- [74] G. Marsaglia. *PNAS*, 61(1):25–28, 1968.
- [75] W. Paul B. Dünweg. *Int. J. Mod. Phys. C.*, 2(3):817–827, 1991.
- [76] V. Ramasubramani et al. *Comput. Phys. Commun.*, 254:107275, 2020.

- [77] S. L. Altmann. *Mat. Mag.*, 62(5):291–308, 1989.
- [78] J. Voight. graduate texts in mathematics. springer, 2022.
- [79] A. P. Thompson et al. *J. Chem. Phys.*, 2009.
- [80] W. Humphrey et al. Vmd - visual molecular dynamics. *J. Molec. Graphics.*, 1996.
- [81] P. G. Bolhuis et al. *J. Chem. Phys.*, 107(5):1551–1564, 1997.
- [82] D. Frenkel et al. *Nature*, pages 822–823, 1988.
- [83] D. Frenkel P. Bolhuis, 1997.
- [84] M. Bagnani et al. *Soft Matter*, pages 2158–2169, 2021.
- [85] P. C. Millett J. T. Jack. *AIP Advances*, 11(2), 2021.
- [86] Louis Kang. Chirality and its spontaneous symmetry breaking in two liquid crystal systems. 2015.
- [87] B. Jerome. *Rep. Prog. Phys.*, 1991.
- [88] J. V. Selinger. Soft and Biological Matter. 2016.
- [89] L. Tortora Oleg D. Lavrentovich. *PNAS*, 108:5163–5168, 2011.
- [90] Z. S. Davidson et al. *Phys. Rev. E*, 2015.
- [91] L. Verlet. *Phys. Rev.*, 159:98–103, 1967.
- [92] W. C. Swope et al. *Chem. Phys.*, 76:637–649, 1982.
- [93] S. Tremaine G. D. Quinlan. *R.Astron.Soc.*, pages 505–518, 1992.
- [94] V.I. Arnol'd. Springer-Verlag, 2nd edition, 1989.

Appendix A

Integrating Newton's Equations of Motion.

Lots of algorithms have been used to do this with varying degrees of complexity. The most common is the Verlet Algorithm [91], which does not directly use velocity. The algorithm we use in LAMMPS is the Velocity-Verlet algorithm. The derivation of this found below is built on the work of [92]. First, consider a particle in an MD simulation, assuming Newton's second law [34] with no relativistic effects, it follows

$$\mathbf{a}_n = \frac{\mathbf{f}(t_n)}{m}, \quad (\text{A.1})$$

where \mathbf{a}_n is the acceleration at time t_n , $\mathbf{f}(t_n)$ is the force at time t_n , τ_n is the position and m is the mass of the particle. Let h be the integration timestep, it follows that

$$t_n = nh, \quad (\text{A.2})$$

$$\tau_n = \tau(t_n), \quad (\text{A.3})$$

$$\mathbf{v}_n = \mathbf{v}(t_n), \quad (\text{A.4})$$

where \mathbf{v}_n is the velocity of the particle at time t_n . We now use a Taylor expansion of the coordinate of a particle around time, t_n to the 4th power,

$$\tau_{n+1} = \tau_n + \mathbf{v}_n h + \frac{\mathbf{f}(\tau_n)}{2m} h^2 + \frac{\dot{\mathbf{f}}(\tau_n)}{3!} h^3 + \Theta(h^4). \quad (\text{A.5})$$

Similarly,

$$\tau_{n-1} = \tau_n - \mathbf{v}_n h + \frac{\mathbf{f}(\tau_n)}{2m} h^2 - \frac{\dot{\mathbf{f}}(\tau_n)}{3!} h^3 + \Theta(h^4). \quad (\text{A.6})$$

We now implement the "summed form" ,

$$z_n = \frac{\tau_{n+1} - \tau_n}{h}, \quad (\text{A.7})$$

it can be shown that

$$\tau_n = \tau_{n-1} + h z_{n-1}, \quad (\text{A.8})$$

and

$$z_n = z_{n-1} + h \mathbf{f}(\tau_n). \quad (\text{A.9})$$

These equations are then applied from $n : 0 \rightarrow M$, where M is the final timestep.

Velocities can be obtained as

$$\mathbf{v}_n = \frac{(z_n + z_{n-1})}{2}. \quad (\text{A.10})$$

These equations are mathematically equivalent to the Verlet algorithm , [29], but are not numerically equivalent and are in fact more accurate on a finite precision basis. The Velocity-Verlet has velocity directly in the calculation equations unlike in the regular Verlet algorithm. The velocity calculation follows as

$$\mathbf{v}_{n+1} = \mathbf{v}_n + \frac{h}{2m} [\mathbf{f}(\tau_{n+1}) + \mathbf{f}(\tau_n)] + \frac{2h^2}{3} [\dot{\mathbf{f}}(\tau_{n+1}) + \dot{\mathbf{f}}(\tau_n)] + \Omega(h^4). \quad (\text{A.11})$$

The mathematical equivalence of Verlet and Velocity-Verlet [29, 92] are such that the error terms are identical,

$$\delta\tau = \Omega(h^4) \text{ and } \delta\mathbf{v} = \Omega(h^2). \quad (\text{A.12})$$

The summed form of velocity and position have superior numerical precision, as we are obtaining the position and velocity at the end of the timestep from the position and velocity at the beginning of the timestep, which means that we calculate the velocities and positions at equal times, unlike the Verlet Algorithm which computes velocity after the position. A Verlet-type algorithm is suitable for almost any simulation. However, those that require more precision can use higher order algorithms which are necessarily more time consuming. This method is time reversible and conserves linear momentum, while showing good energy conservation for longer simulations. Verlet-style algorithms struggle with short term energy stability. It would be desireable to use an alogorithm which works on both the short and long timescales but unfortunately no such general algorithm

for this yet exists, [29].

We would expect that during MD integration errors would eventually compound and lead to exponential divergence of the simulated trajectories from the true trajectories with the same initial conditions. This is known as the Lyapunov's instability [29]. In practise, these errors are not of great concern because we use MD for a statistical prediction, not exact trajectory observations.

MD is still only justified in the case that the numerical predictions are somewhat close to the true trajectories. While this is not proven, it is generally true, for strong numerical evidence of this, see [93]. For a long time period, true trajectory generally follows a numerical trajectory called the shadow orbit. Provided this time is long enough, we can avoid the Lyapunov's Instability.

Earlier we mentioned the time-reversible nature of Verlet-style algorithms. This is an important feature because Newton's laws of motion are time reversible. Furthermore, the reversibility is crucial in the preservation of the volume element in Hamiltonian mechanics, [94]. Most algorithms that are not time reversible do not reproduce the area preserving property, meaning that the volume of phase space is not preserved and after a long period of time this will lead to an expanded system that violates energy conservation. Reversible, area preserving algorithms are not guaranteed to feature no energy drift. However, their drift's are in general far smaller in magnitude and effect than non-area preserving algorithms.

In summary, Verlet-like algorithms are fast and have low memory requirements but are not accurate for large timesteps, so frequent force calculation is required. The algorithm's short term energy accuracy is fair but long term energy drift is very low. They are time-reversible and area preserving and accurate enough that for most systems the Lyapunov instability will not be a concern.

Appendix B

The Volume of Overlap of Two Parallel Rods.

The volume of overlap of two parallel cylinders ($V_{\text{cylinder}}(r)$), see Figure ??, is

$$V_{\text{cylinder}}(r) = L \times A_{\text{overlap}}(r), \quad (\text{B.1})$$

where L is the length of the cylinder of the rod and $A_{\text{overlap}}(r)$ is the overlap area of two circles, see Figure B.2.

The cross-section of the cylinders is the area of overlap is two congruent chords, expressed as

$$A_{\text{overlap}}(r) = \sigma_{\text{rd}}^2(\theta - \sin\theta), \quad (\text{B.2})$$

This area and the notation is shown in Figure ??, where $\theta = \arccos\left(\frac{r}{2\sigma_{\text{rd}}}\right)$. Combining θ with (B.2) and (B.1) gives

$$V_{\text{cylinder, overlap}}(r) = L\sigma_{\text{rd}}^2 \left[2\arccos\left(\frac{r}{2\sigma_{\text{rd}}}\right) - \sin\left(2\arccos\left(\frac{r}{2\sigma_{\text{rd}}}\right)\right) \right]. \quad (\text{B.3})$$

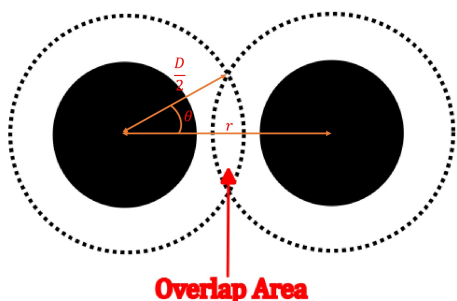


Figure B.1: This Figure shows the cross-sectional slice of Figure B.2

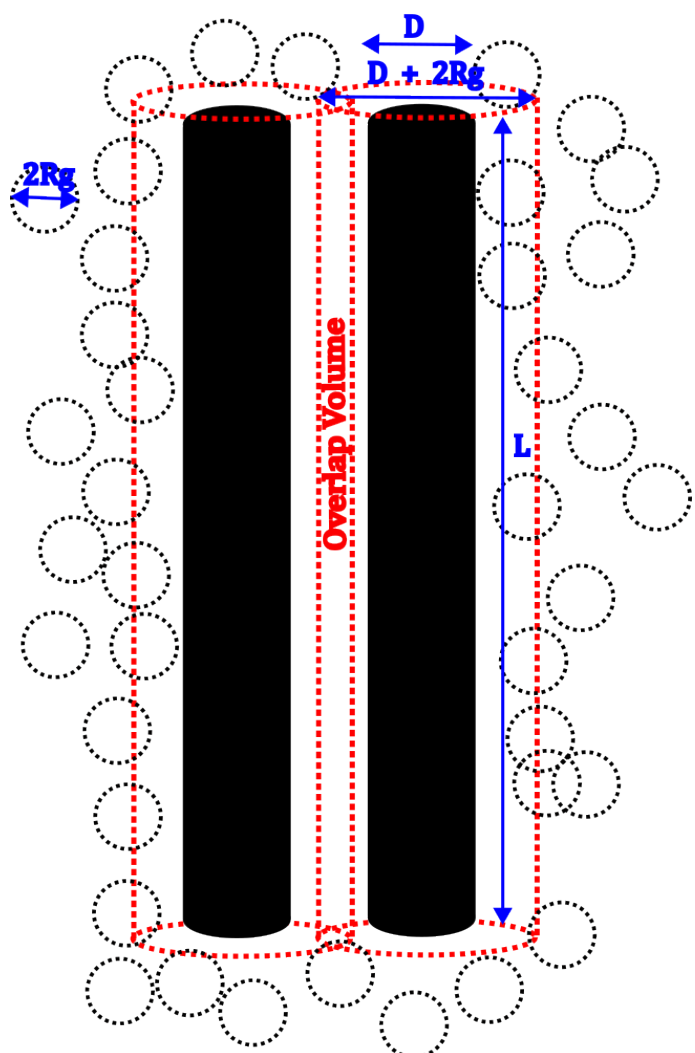


Figure B.2: This Figure displays the depletion overlap volume of two parallel cylinders.

Appendix C

Scaled Particle Theory of Finite Sized Rods

In this section we will use SPT to discuss the isotropic-nematic transition for finite sized rods. For a wider account of the origin of SPT for a dispersion of rods, see [9].

SPT, is a convenient way to incorporate higher virial coefficients for the treatment of the isotropic - nematic phase transition. To start with SPT we have to calculate the reversible work, $W(\omega, \lambda, \sigma)$, to insert an additional spherocylinder in the system of spherocylinders. Here, λ and σ scale the length and diameter respectively of the inserted spherocylinder. $\lambda = 1$ and $\sigma = 1$ means we are inserting a spherocylinder of the same dimensions as the system of spherocylinders. Inserting an additional spherocylinder in the system of spherocylinders using $W(\omega, 1, 1)$ gives the excess chemical potential

$$\mu^{\text{ex}} = \int f(\omega) W(\omega, 1, 1) d\omega, \quad (\text{C.1})$$

where $W(\omega, 1, 1)$ is the reversible work to insert a spherocylinder of orientation ω , length L and diameter D into a system of hard spherocylinders. The expression for $W(\omega, 1, 1)$ follows from SPT [9]. We obtain

$$W(\omega, 1, 1) = \left(\frac{1}{6} \pi D^3 + \frac{1}{4} \pi D^2 L \right) P^R, \quad (\text{C.2})$$

where P^R is the pressure of the rod reservoir as determined by FVT.

The expression (??) for μ^{ex} was derived from the isotropic system of rods but can be applied equally well to the nematic phase of rods, just with a $f(\omega)$ that matches the nematic phase. Replacing the second virial contribution $2c\rho[f]$ in (??) with μ^{ex} , we obtain

$$\frac{\mu}{kT} = \text{constant} + \ln y + \sigma[f] + (1 + 2A[f])y + \left(A[f] + \frac{3}{2}B[f]\right)y^2 + B[f]y^3, \quad (\text{C.3})$$

where y takes the form $\frac{\phi}{1 - \phi}$, with ϕ as the volume fraction for the rods as shown in (2.29), but here the excluded volume, ν_0 , is

$$\nu_0 = \frac{\pi}{4}LD^2 + \frac{\pi}{6}D^3. \quad (\text{C.4})$$

The quantities $A[f]$ and $B[f]$ are defined as

$$A[f] = 3 + \frac{3(\gamma - 1)^2}{(3\gamma - 1)}\rho[f], \quad (\text{C.5})$$

$$B[f] = \frac{12\gamma(2\gamma - 1)}{(3\gamma - 1)^2} + \frac{12\gamma(2\gamma - 1)^2}{(3\gamma - 1)^2}\rho[f], \quad (\text{C.6})$$

where, $\gamma = 1 + \frac{L}{D}$. Now using the Gibbs-Duhem equation

$$\left(\frac{\partial P}{\partial n}\right) = n \left(\frac{\partial \mu}{\partial n}\right). \quad (\text{C.7})$$

We obtain the pressure

$$\frac{P\nu_0}{kT} = y + A[f]y^2 + B[f]y^3. \quad (\text{C.8})$$

Finally, we use use $F = N\mu + PV$ to obtain

$$\frac{F[f]}{Nk_bT} = \text{constant}' - 1 + \sigma f \ln y + A[f]y + \frac{1}{2}B[f]y^2 \quad (\text{C.9})$$

where $\text{constant}'$ is,

$$\text{constant}' = \text{constant} + \ln \frac{L}{D}. \quad (\text{C.10})$$

From here we locate the I-N transition and coexistence in the same way as in Section ??.

- i Minimize $F[f]$ numerically wrt f .
- ii Calculate the f .
- iii Calculate pressure and chemical potential of the isotropic and nematic phases.

iv Solve the coexistence conditions for c_l and c_N .

The result of this coexisting condition which now depends on L/D. In the case of L/D $\rightarrow \infty$, the numerical solution converges and fits with the Onsager limit values.

Comparing the Gaussian and Numerical approach shows sufficient agreement in favour of the convenience of the Gaussian method. Using (2.41) as our Gaussian orientational distribution function and substituting (2.42) and (2.43) as $\sigma[f_G]$ and $\rho[f_G]$ respectively then minimizing this wrt κ yields

$$\kappa = \frac{36}{\pi} \frac{(\gamma - 1)^4}{(3\gamma - 1)^2} \left(y + \frac{2\gamma}{3\gamma - 1} y^2 \right)^2. \quad (\text{C.11})$$

Appendix D

LAMMPS Data Generator File

The file below is a typically LAMMPS python data generating file, for a system of 2000 rods with 21 particles per rod.

```
import numpy as np

MDa = 1.66054e-21
Diameter = 7*10**(-9)
atom_types = 1
rod_molecule_number = 2000
particles_in_rod = 21
mass = (10**(-2)*MDa)/particles_in_rod
rod_number = rod_molecule_number*particles_in_rod
particle_number = rod_number

print('#data for rigid rod molecule.')
print(' ')
print(particle_number,'atoms')
# print(' ')
print( atom, 'atom types')
```

```

print(' ')
print('0 0.8e-7 xlo xhi')
print('0 1.6e-7 ylo yhi')
print('0 1.07e-6 zlo zhi')
print(' ')
print('Masses')
print(" ")
print(1, mass)
print(' ')
print('Atoms')
print(' ')
for j in range(0,2000):
    s = j
    quotient = s//200
    remainder = s%200
    quotient_2 = remainder//20
    remainder_2 = remainder%20
    z= 36*10**(-9) + (quotient)**72*10**(-9)
    x= 10*10**(-9) + (quotient_2)**8*10**(-9)
    y= 10*10**(-9) + (remainder_2)**8*10**(-9)
    for i in range(j*particles,(j+1)*particles):
        i=j*particles
        z = z+ (i-i)**3.15*10**(-9)
        x = x
        y = y
        print(i+1,j+1,1,x,y,z)

```

Appendix E

LAMMPS Input Scripts

This script is an example of a typical LAMMPS input script. This script was used to run MD on a long cell tactoid system.

```
# Initialization of the rod and cell systems.
```

```
units si
dimension 3
boundary p p p
atom_style bond
```

```
# Variables.
```

```
variable timestep_1 equal 1e-12
variable timestep_2 equal 2e-12
variable k_b equal 1.3806e-23
variable MDa equal 1.66054e-21
variable binsize equal 2e-8
variable deletion_radius equal 4e-9
variable T equal 300
variable sigma equal 7e-9
variable sigma_1_2 equal 53.5e-9
```

```

variable sigma_2_2 equal 100e-9
variable WCA_2_2_cutoff equal ((2)^(1/6))^{( ${sigma_2_2} ) )
variable WCA_1_1_cutoff equal ((2)^(1/6))^{( ${sigma} ) )
variable lennard_jones_rod_cutoff equal 5e-8
variable lennard_jones_cell_cutoff_nofitting equal 1e-7
variable 2_2_well_depth equal ${k_b} * $T
variable LJ_range equal 1.2e-7
#variable deletion_of_rods equal 35e-9

```

Well Depth Variable values.

```

variable 1_1_well_depth equal 1 * ${k_b} * $T
variable 1_2_well_depth equal 0.5 * ${k_b} * $T

```

The data section.

```
read_data data_long_cell_2000_21_1_11_0.1.txt
```

The potential and pair style.

```

pair_style lj/expand ${LJ_range}
pair_coeff 2 2 ${2_2_well_depth} ${sigma_2_2} 0 ${WCA_2_2_cutoff}
pair_modify shift yes
pair_coeff 1 1 ${1_1_well_depth} ${sigma} 0 ${WCA_1_1_cutoff}
pair_modify shift yes
pair_coeff 1 2 ${1_2_well_depth} ${sigma_1_2} 0 ${lennard_jones_cell_cutoff_nofitting}

```

Neighbor Modification.

```
neighbor ${binsize} bin  
neigh_modify every 1 delay 10  
neigh_modify one 100000  
neigh_modify page 1000000  
comm_modify cutoff 5e-7
```

Groups.

```
group rigid_bodies type 1  
group rigid_cell type 2
```

Modify.

```
neigh_modify exclude molecule/intra rigid_bodies  
neigh_modify exclude molecule/intra rigid_cell
```

Fixes.

```
fix rigid_bodies_fix rigid_bodies rigid/small molecule langevin $T $T 100${timestep_1}  
10000 reinit no  
fix rigid_cell_fix rigid_cell rigid/small molecule langevin $T $T 100${timestep_1} 10000  
reinit no  
# Velocity setup.
```

```
velocity all create $T 10000 rot yes dist gaussian  
run 0  
velocity all scale $T
```

Deletion.

```
delete_atoms overlap ${deletion_radius} rigid_bodies rigid_bodies

# Thermodynamic Data collection.

thermo_style custom step temp press ke pe etotal atoms vol
thermo 100

dump mydmp all atom 1000 visualisation_long_cell_2000_21_1_11_0.5_WCA_500000.lammpstrj
log log_rod_and_cell_2000_21_1_11_0.5_WCA_500000.lammps

# Computation of Quaternion Data.

compute Quaternion_Calculation rigid_bodies rigid/local rigid_bodies_fix mol quatw quat
quatj quatk

dump Quaternion_Calculation_Rod_noID_Dump_File rigid_bodies local 5000 Quaternion_long_cell_rod_2000_21_1_11_0.5_WCA_50000.data c_Quaternion_Calculation[2]
c_Quaternion_Calculation[3] c_Quaternion_Calculation[4] c_Quaternion_Calculation[5]

# Computation of atomic position data.

dump atomic_coordinates_dump rigid_bodies custom 5000 tactoid_coordinate_data_long_cell_0.5_
WCA.atom id mol type x y z

# Running the system.

minimize 0 0 1000 100000
timestep ${timestep_1}
```

```
run 10000  
timestep ${timestep_2}  
run 500000
```

Appendix F

The Critical Endpoint

At various q and L/D ratios, the existence of multiple isotropic and nematic phases has to be considered. For this system we fall within the isotropic and nematic region as indicated by the red point in Figure F.1 meaning the $I_1 + I_2$ or $N_1 + N_2$ coexistence phases do not have to be considered as there are no critical points for the isotropic and nematic phases within this region. For more detail, see [9].

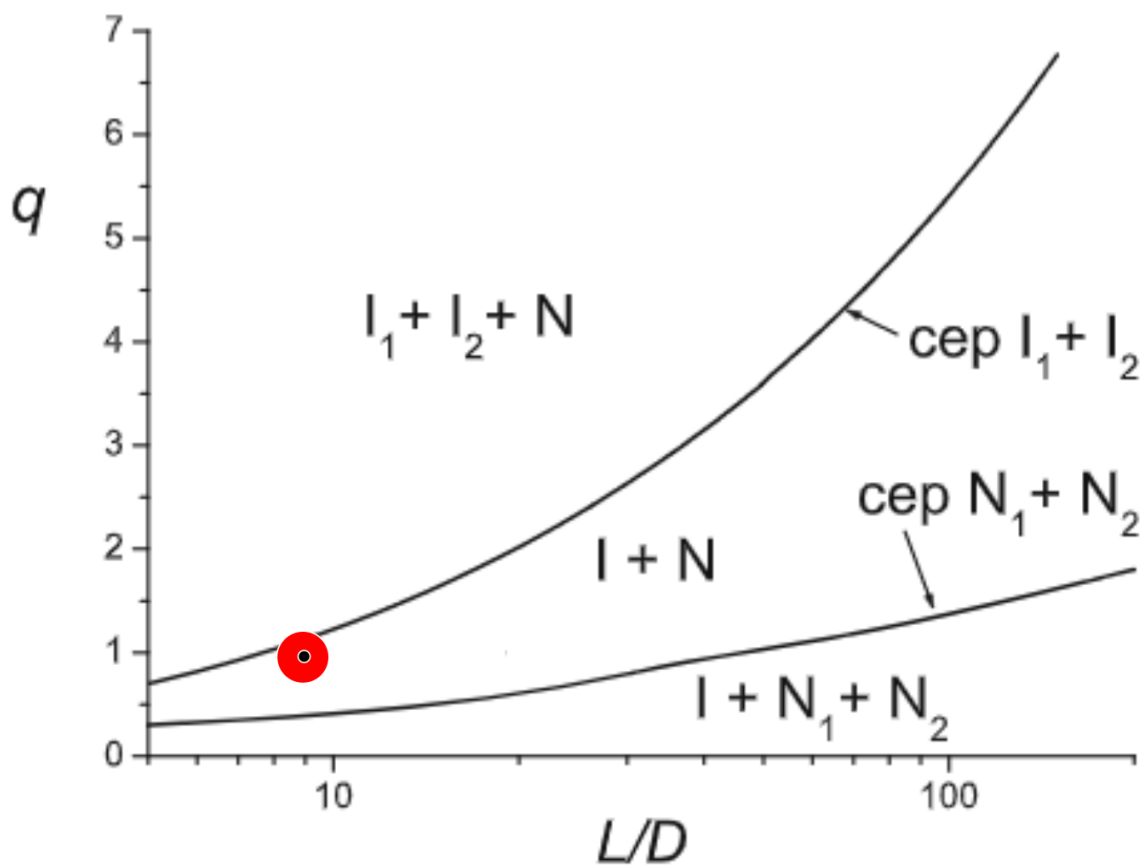


Figure F.1: This Figure, taken from [9], gives the position of our system on the Critical Endpoint diagram. These lines are determined using the Gaussian orientational function [9]. The black lines are the CEP curves of $I_1 + I_2$ and $N_1 + N_2$, the red point is the $(L/D, q)$ values of our system. This shows that our system is within the $I + N$ region, so we do not have to consider an I or N critical points.